Images and their analysis

... proves nothing. Often a hen merely lays an egg and cackles as if she has laid an asteroid.

Mark Twain.

Following the Equator

Chapter 5

IMAGES AND THEIR ANALYSIS

·5.1   Introduction

In this chapter we present images spanning one hour in RA and the full declination range of the MRT with a resolution of 4' x $9'.2 \sec(\delta + 20°.14)$. We also present an analysis of these images and compare our results with the data from the Molonglo Reference Catalog[1] (MRC) [40].

We particularly chose the region between 19 hrs and 20 hrs in RA, which has our calibrator MRC 1932-464, for making the first full declination image from the MRT using the recirculator data. The region imaged is shown by hatched lines in Figure **5.2.** This helps us in the flux density calibration of the other sources in the image. Comparison of the estimates of the flux density and the positional information of these sources with the existing data helps us

---

[1]The Molonglo Reference Catalog (MRC) has been prepared from the 408-MHz survey observations made with the Molonglo Radio Telescope. The resolution of the telescope is $2'.62$ x $2'.86 \sec(\delta + 30°.5)$. The pointing and the flux density calibration of this catalog are based on measurements of Hunstead [38] and an absolute scale of Wyllie [39]. The survey covers 7.85 sr of the sky defined by $+18°.5 \geq \delta(1950) \geq -85°.0$, $|b|$ **3** 3°. The catalog comprises celestial coordinates with standard error typically lying between 3 and 10 arcsec and 408-MHz flux densities with standard error typically lying between 4 and 10 per cent. The overall source density is 1500/sr, corresponding to 0.001 per beam area. There are 7347 sources of listed flux density ≥ 1.00 Jy, at which level the catalog is substantially complete. The reliability is believed to be better than 99.9 per cent.

Chapter 5: Images and their analysis
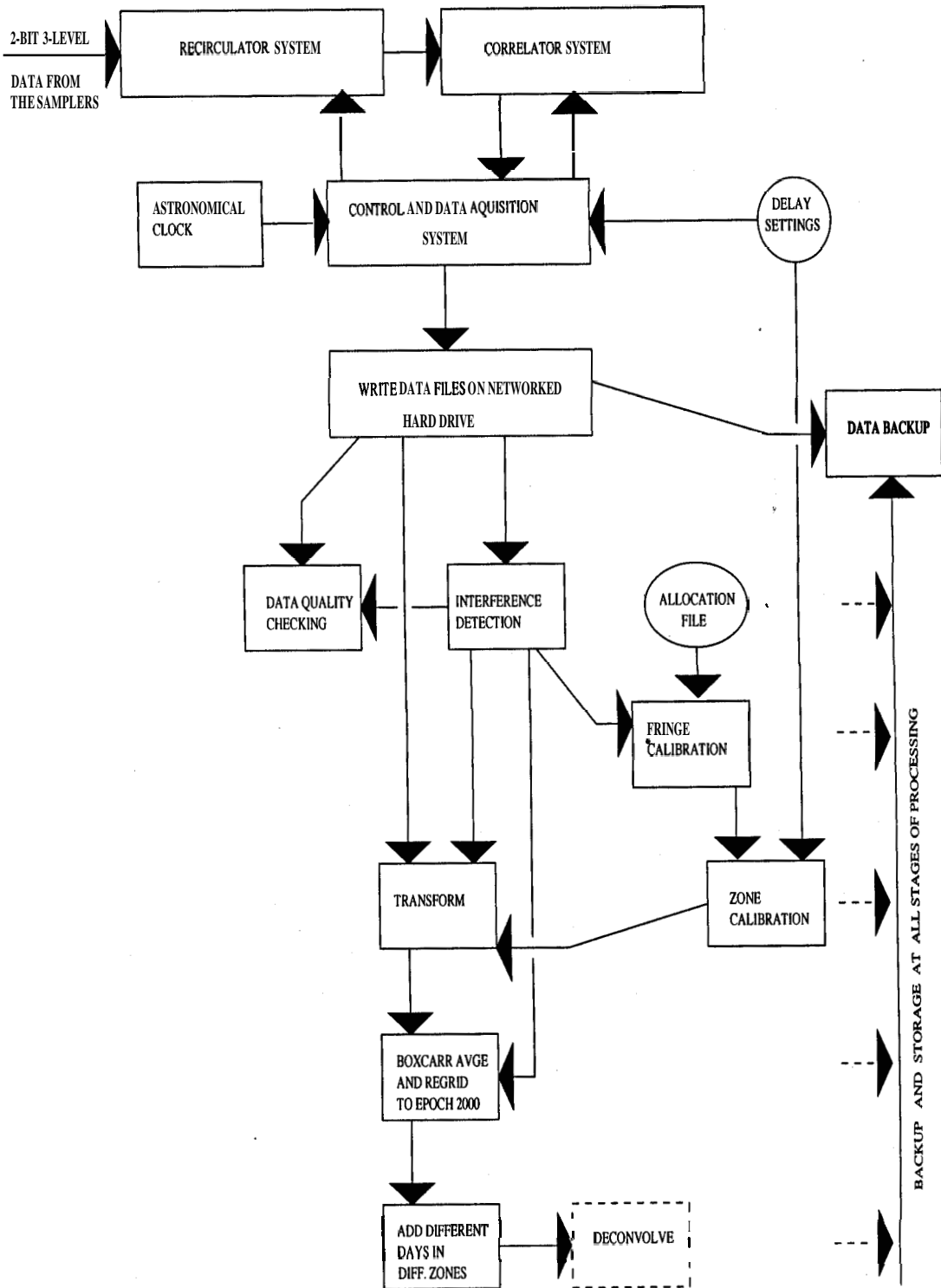
Figure 5.1: A schematic showing various data processing stages involved in getting the final images.
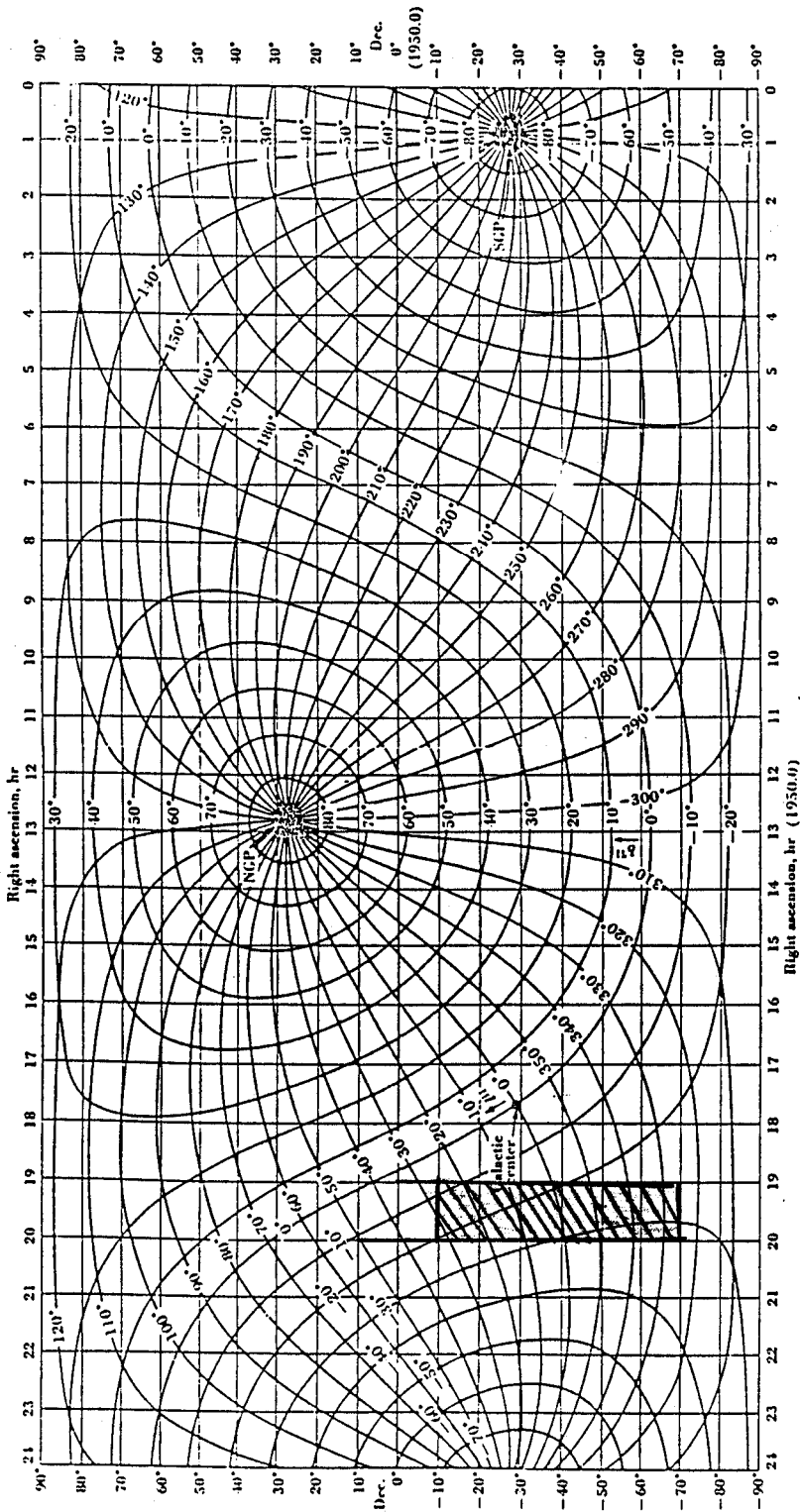
Figure 5.2: Chart for conversion of equatorial (1950) coordinates into new galactic coordinates [3]. The region imaged is shown as hatched lines.

gain confidence in the various tools used for imaging. These images use north-south baselines only up to 441 m, i.e., about the mid-point in the north-south arm. We believe that all the required techniques to make the full resolution dirty images with the MRT have been demonstrated.

5.2 Wide field images with a resolution of $4' \times 9'.2 \sec(\delta + 20°.14)$

5.2.1 Data processing

The data for all the baselines were collected over a time span of two years. The data used for baselines up to 172 m were obtained in the period July 1994 to September 1994. The data for baselines from 172 m to 441 m were obtained during the period September 1995 to April 1996. Observations with baselines 442 m to 711 m were carried out in the period April 1996 to July 1996 and data with baselines 712 m to 880 m were obtained in the period August 1996 to November 1996. We collected more than 120 Giga bytes of data in the first round of observations. Visibility measurements using north-south baselines of up to 441 m with all the **32** groups of the east-west array are used in the images presented here.

The visibilities measured with different delay settings go through several stages of processing before the images are made. They have been described in the previous chapters and are summarized below[2]. Figure 5.1 is a schematic of the processing stages involved.

- Visibilities were measured with different delay settings

---

[2]The most time consuming process is that of extracting the data from some 150 tapes (8 mm) and identifying the good data. The data has been stored as 24 hour sets. We are now in the process of storing the data on an hourly basis and producing an easy-to-use data-base which will help to reduce this overhead in time required for locating good data for imaging.

For north-south baselines up to 172 m we did not use the recirculator. For baselines shorter than 172 m the bandwidth decorrelation is within 15% over the declination range covered by the primary beam of the helix. For north-south baselines of 172 m to 261 m (block-3), the visibilities were measured with 2 different delays. For baselines of 262 m to 351 m (block-4), the visibilities were measured with 3 different delays. For baselines of 352 m to 441 m (block-5), the visibilities were measured with 4 different delays.

- Interference detection (Section 4.1) was carried out on all the data. The detected points were stored and used to reject the data corrupted by interference in subsequent processing.

- On each day of observation, the instrumental complex gain was obtained using the available calibrators (Section 4.2.1). Errors in antenna positions (Section 4.2.4) and in the time stamping (Section 4.2.3) were estimated by comparing the instrumental phases obtained from calibrators at different zenith angles.

- The complex antenna gains estimated using visibilities in one delay zone, in which we have a calibrator, were used to calibrate the instrumental complex gains in the other delay zones (Section 4.2.5).

- On each day, the calibrated visibilities with different delay settings were transformed (Section 4.3.2) separately and box-car averaged for 4 seconds. Interference excision was incorporated at this stage by giving zero weighting to the points corrupted by interference.

- The images of different days were precessed to a common epoch, which

is chosen to be close to the midpoint in time of the duration of the observations (Section 4.4).

- The precessed images of a block (six allocations) in the same delay zone were added. This gave images for different zones in each block (Section 4.4).

- To keep the average bandwidth decorrelation to less than 5%, we made four sets of images by combining images of block-1 and block-2 with images from appropriate delay zones in block-3, block-4 and block-5 (Section 4.4).

- To obtain an optimum signal-to-noise ratio, the four sets of images were convolved in right ascension with a *sinc* function having a FWHM[3] of 16 seconds in time. This is the FWHM in RA of the expected PSF at $\delta = 0$.

- To obtain the estimates of position and amplitude of the point sources given in the MRC, the expected (theoretical) two-dimensional beam was least-square fitted around the position of the point sources given in the MRC.

- The flux density scale was obtained by making a best fit of the helix primary beam in declination to the ratio of flux densities of a large number of sources measured at the MRT and the MRC/Culgoora[4] sources.

---

[3]Since a source at a larger declination spends more time in the beam, a declination-dependent beam in RA may be used for convolving to get the best signal-to-noise ratio.

[4]The updated Culgoora catalog [41] gives list of sources that were observed with the Culgoora Circular Array (CCA) in the interval 1970-1984. The list contains all the sources that were published in the Culgoora-1,2,3 Lists plus additional sources resulting from a survey of 353 Abell clusters of galaxies. The observations were made at 80 **MHz** and 160 **MHz** with HPBW in RA of $3'.70$ and $1'.85$ respectively. The beamwidth in declination is wider by $\sec(30°.3 + S)$. This list brings together all CCA measurements of flux density, position,

We discuss the flux density calibration and estimates of positions and flux densities of the point sources in the following sections.

5.2.2   Flux density calibration

The Baars et al. [42] flux density scale is widely accepted as being the most reliable one available for frequencies up to 30 GHz. The Baars scale is based on the absolute flux density measurements of Cas A and has a list of several secondary calibrators distributed in RA. The calibrators however are all in the northern hemisphere and cannot be used directly to calibrate the flux densities in the MRT survey.

The RBC[5] scale [43] is another widely used flux density scale. This is based on the observations of 225 sources at 10 and 22 MHz by the Dominion Radio Astrophysical Observatory . The flux density scale of the Cambridge 6C survey is based on the RBC scale. Again, 6C is a northern sky survey $(\delta \geq 30°)$, and therefore cannot be used directly for the flux density calibration of the MRT sources.

Because there was no direct way to link the MRT flux density to the available standard flux scales, the flux density calibration at the MRT was carried out in two stages [18] while carrying out a low resolution survey with the MRT.

The flux density of MRC 1932-464 was estimated from the 160 MHz flux density quoted in the Culgoora catalog [41] using a spectral index of 0.7. This gave the flux density of MRC 1932-464 to be 81 Jy/beam at 151.5 MHz. Using this, the flux densities of other point sources in the MRT survey were estimated.

spectral index and angular size, with limiting flux densities of 4 Jy at 80 MHz and 2 Jy at 160 MHz. The sources were selected for CCA observations from the Parkes, 4C and Ohio catalogs if an extrapolation of the then existing spectral data indicated that the 80 MHz flux density would be > 5 Jy.

[5]Roger, Bridle and Costain.
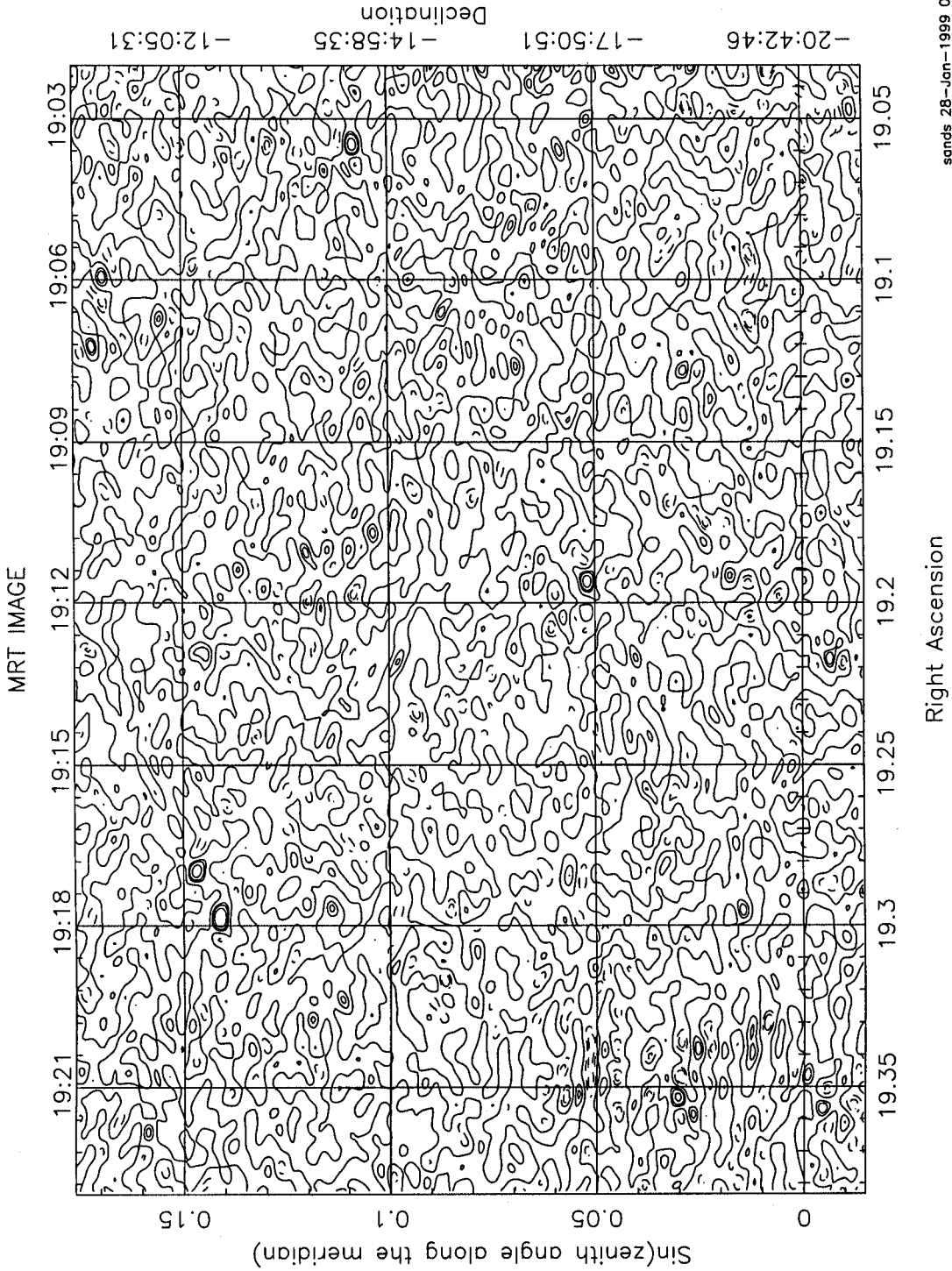
Figure 5.3: Map of the right ascension range (J2000) 19h02m to 19h23m and declination range (52000) −21° to −10°.
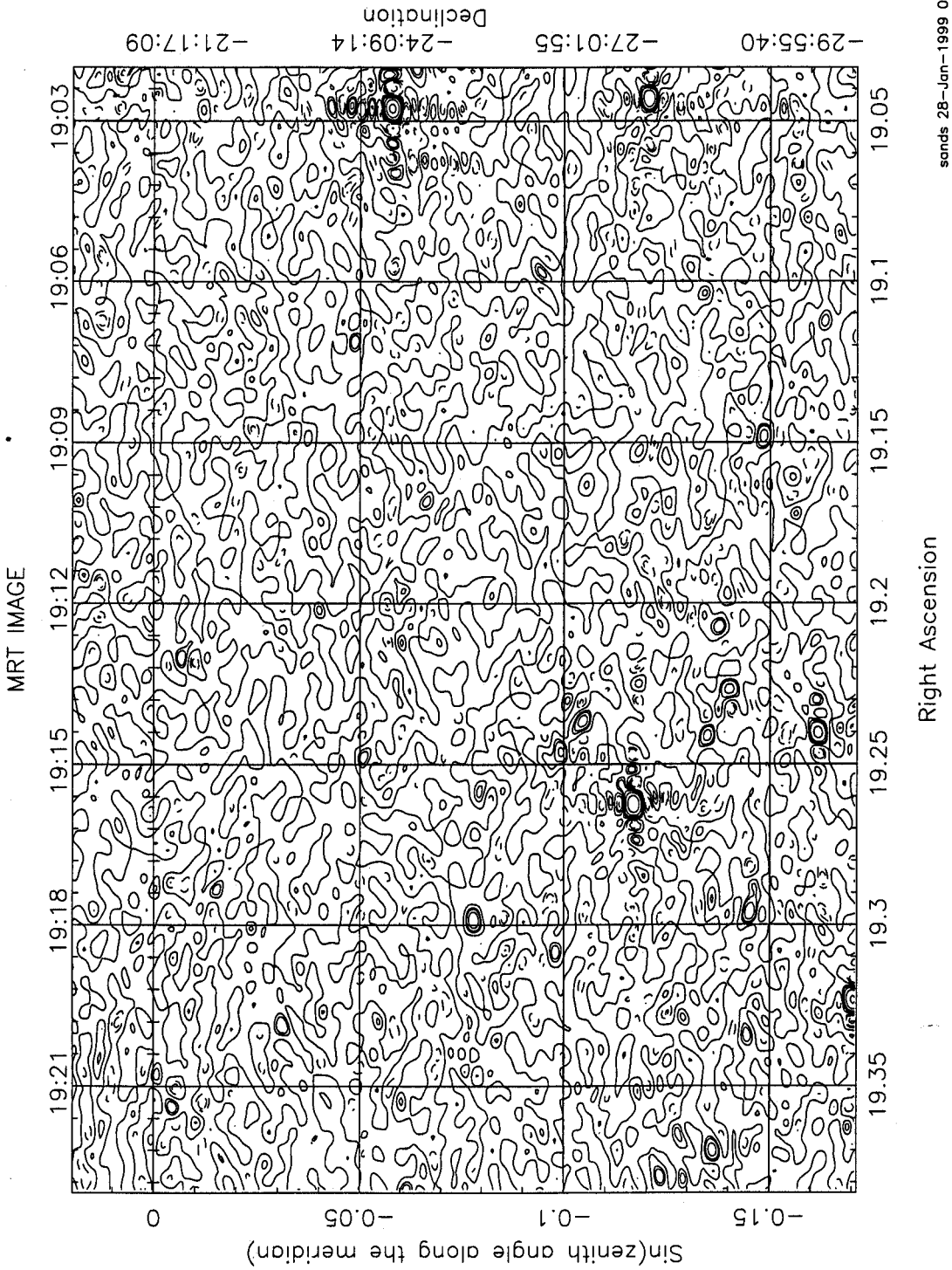
Figure 5.4: Map of the right ascension range (J2000) 19h02m to 19h23m and declination range (J2000) −30° to −19°.
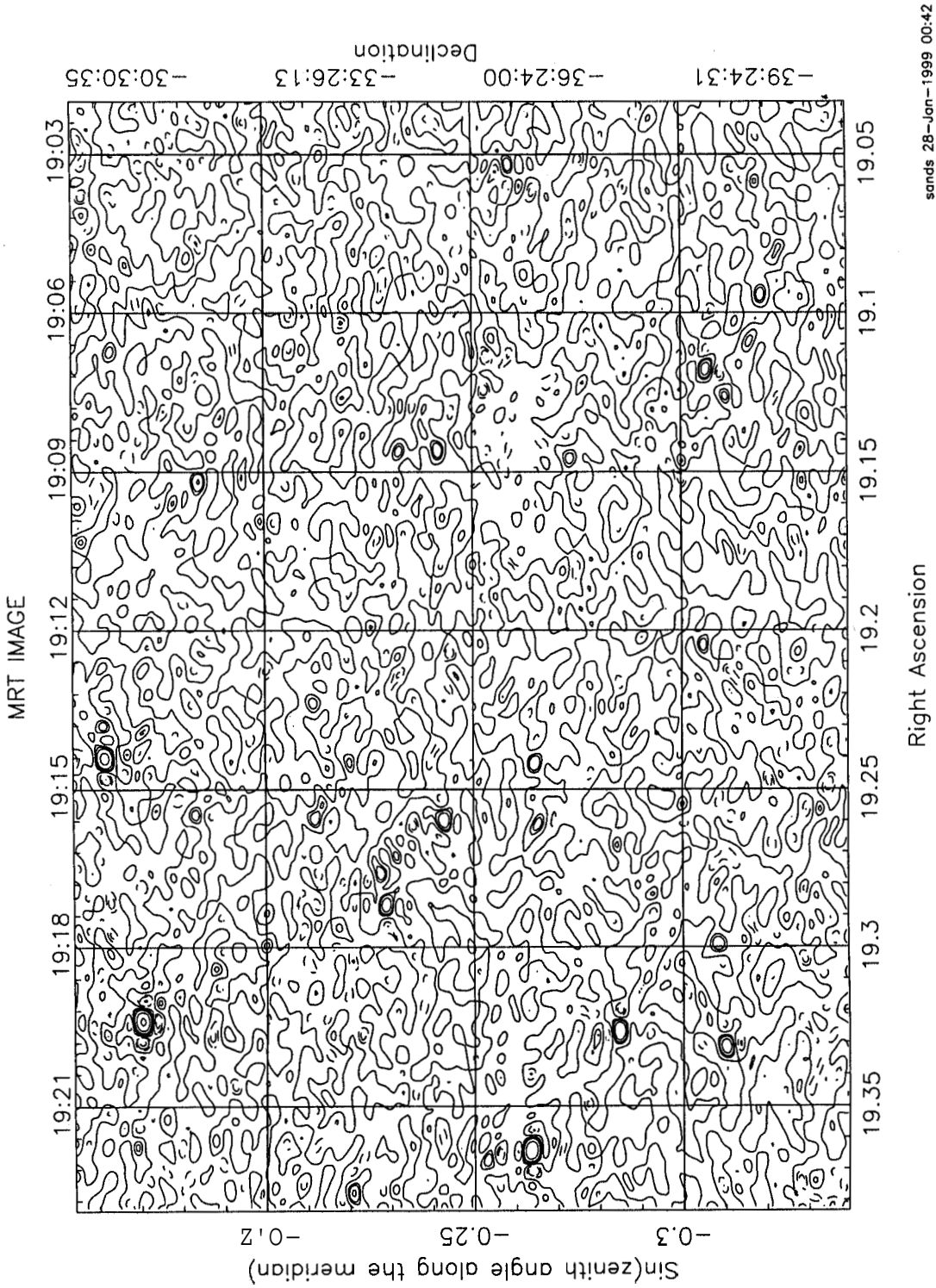
Figure 5.5: Map of the right ascension range (J2000) 19h02m to 19h23m and declination range (92000) −40° to −29°.

Figure 5.6: Map of the right ascension range (J2000) 19h02m to 19h23m and declination range (52000) −50° to −39°.
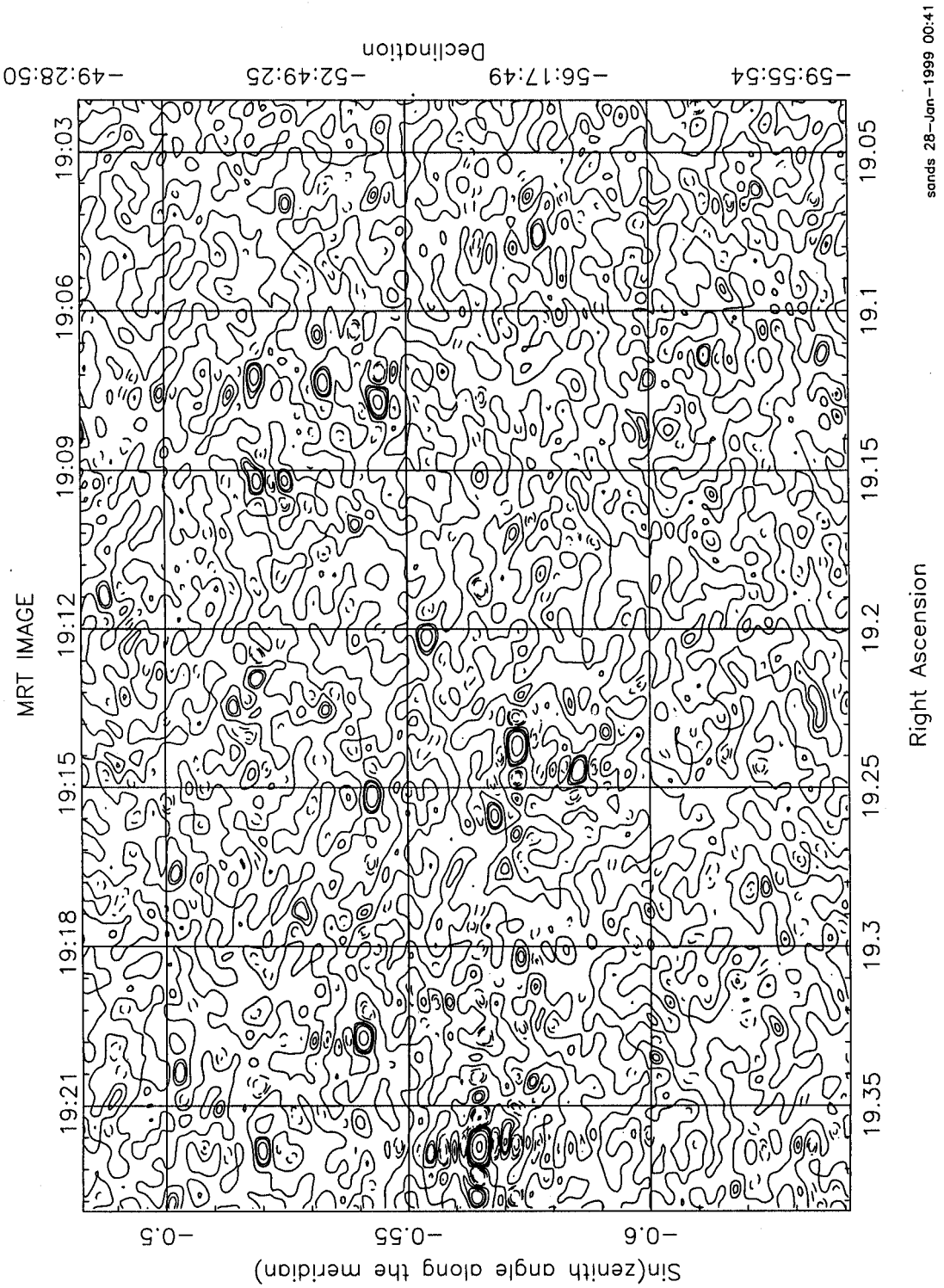
Figure 5.7: Map of the right ascension range (52000) 19h02m to 19h23m and declination range (52000) −60° to −49°.
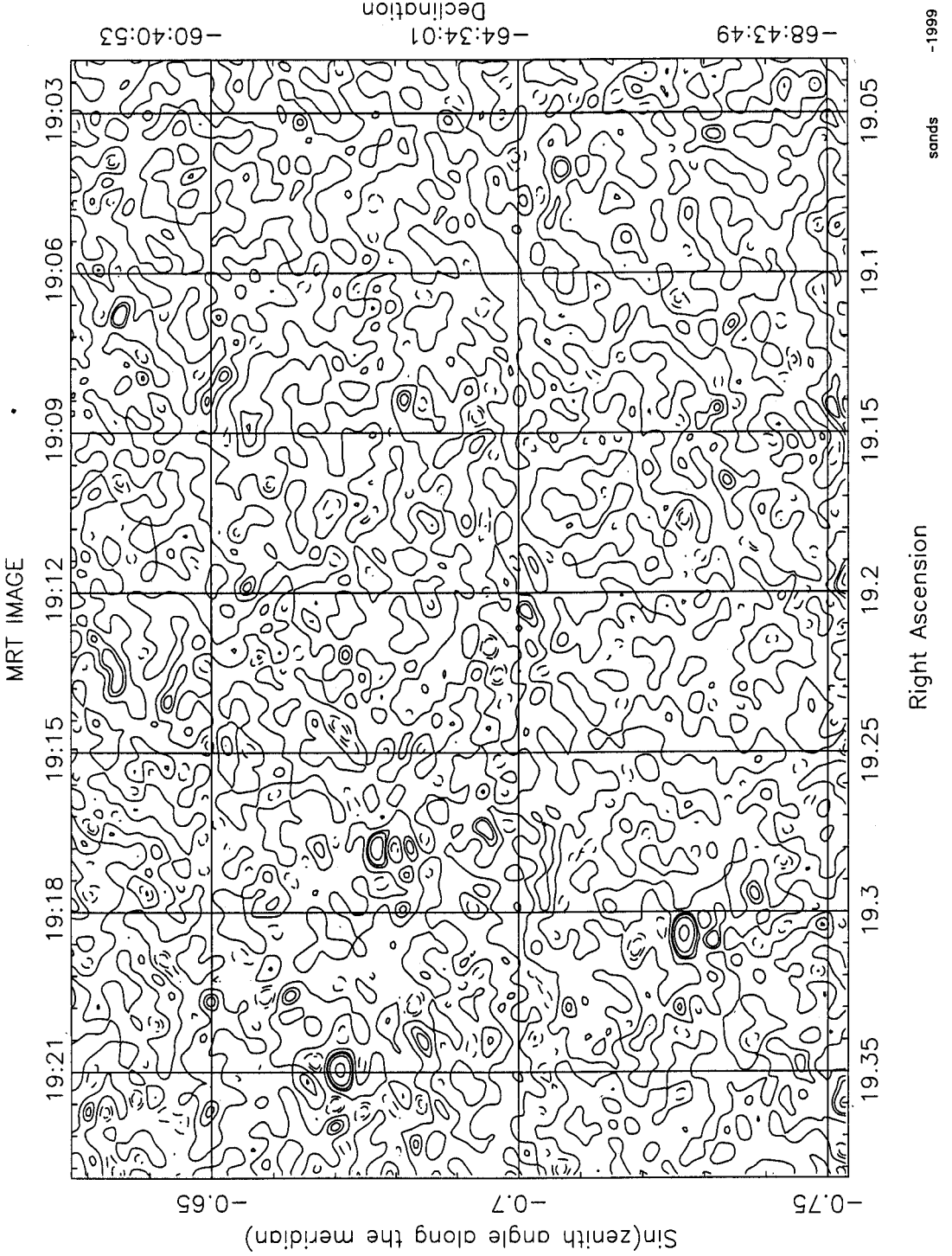
Figure 5.8: Map of the right ascension range (52000) 19h02m to 19h23m and declination range (52000) −70° to −59°.
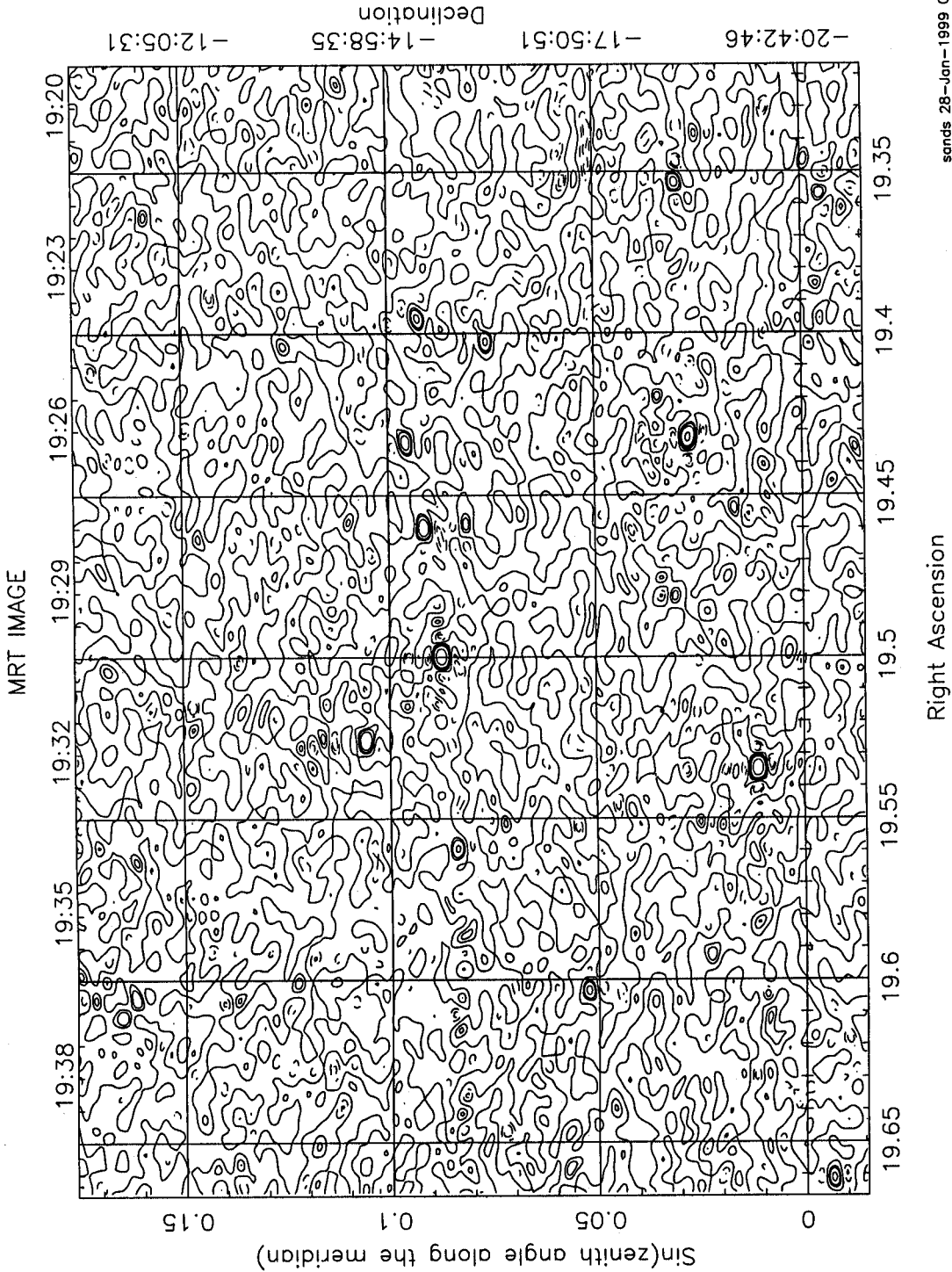
Figure 5.9: Map of the right ascension range (J2000) 19h19m to 19h40m and declination range (J2000) −21° to −10°.
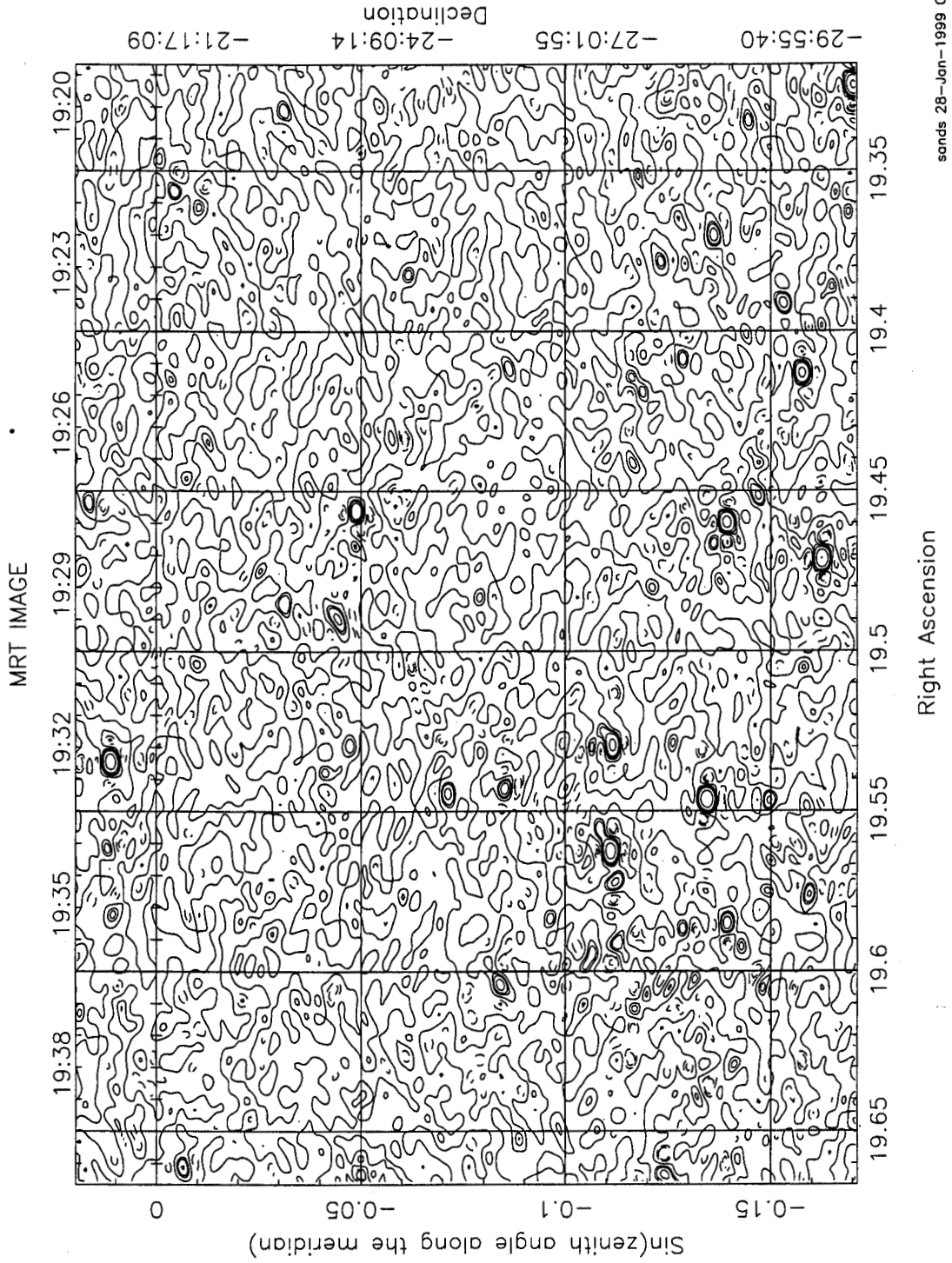
Figure 5.10: Map of the right ascension range (J2000) 19h19m to 19h40m and declination range (J2000) −30° to −19°.

Chapter 5: *Images and their analysis*
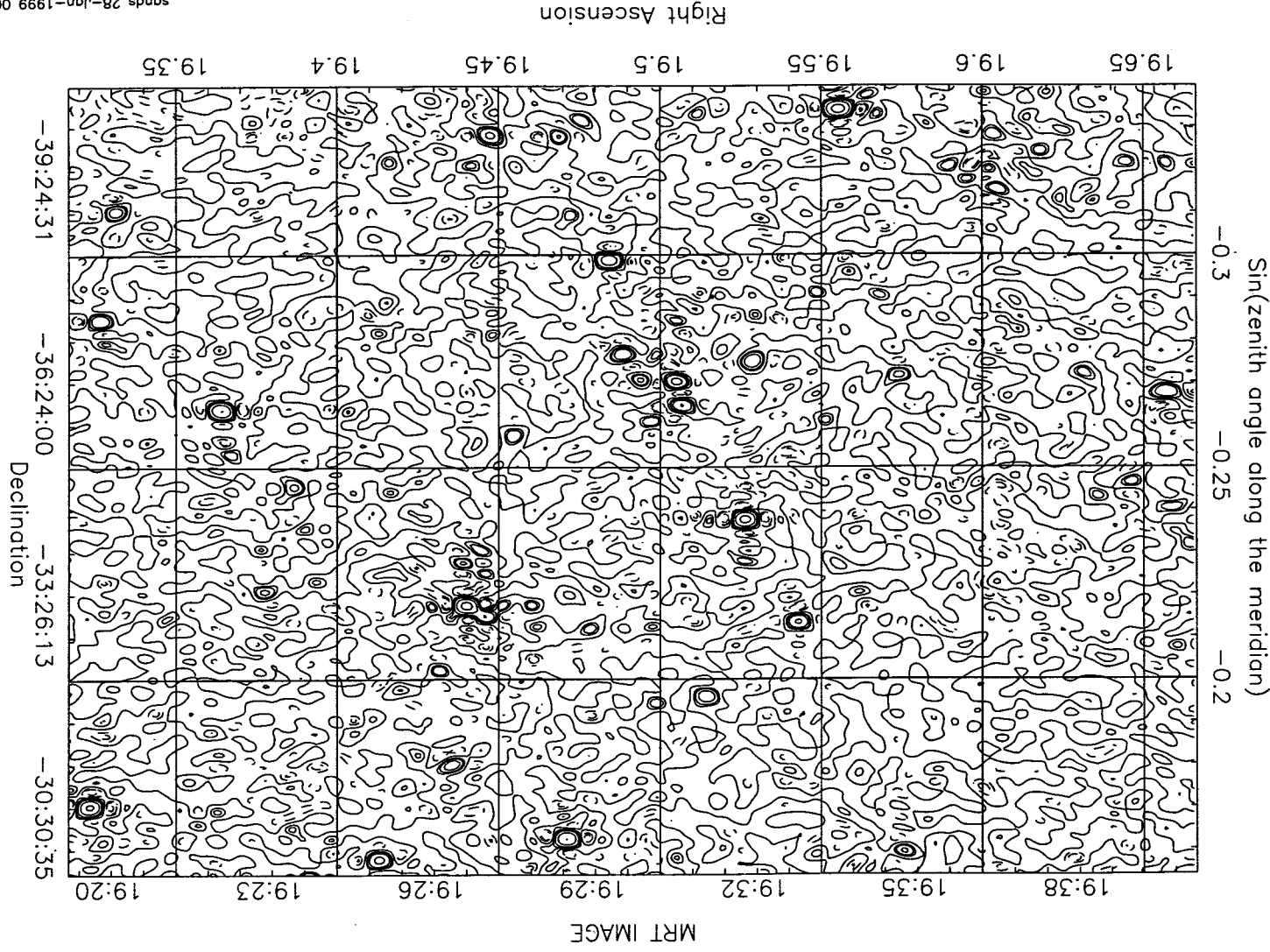
Figure 5.11: Map of the right ascension range (J2000) 19h19m to 19h40m and declination range (J2000) −40° to −29°.
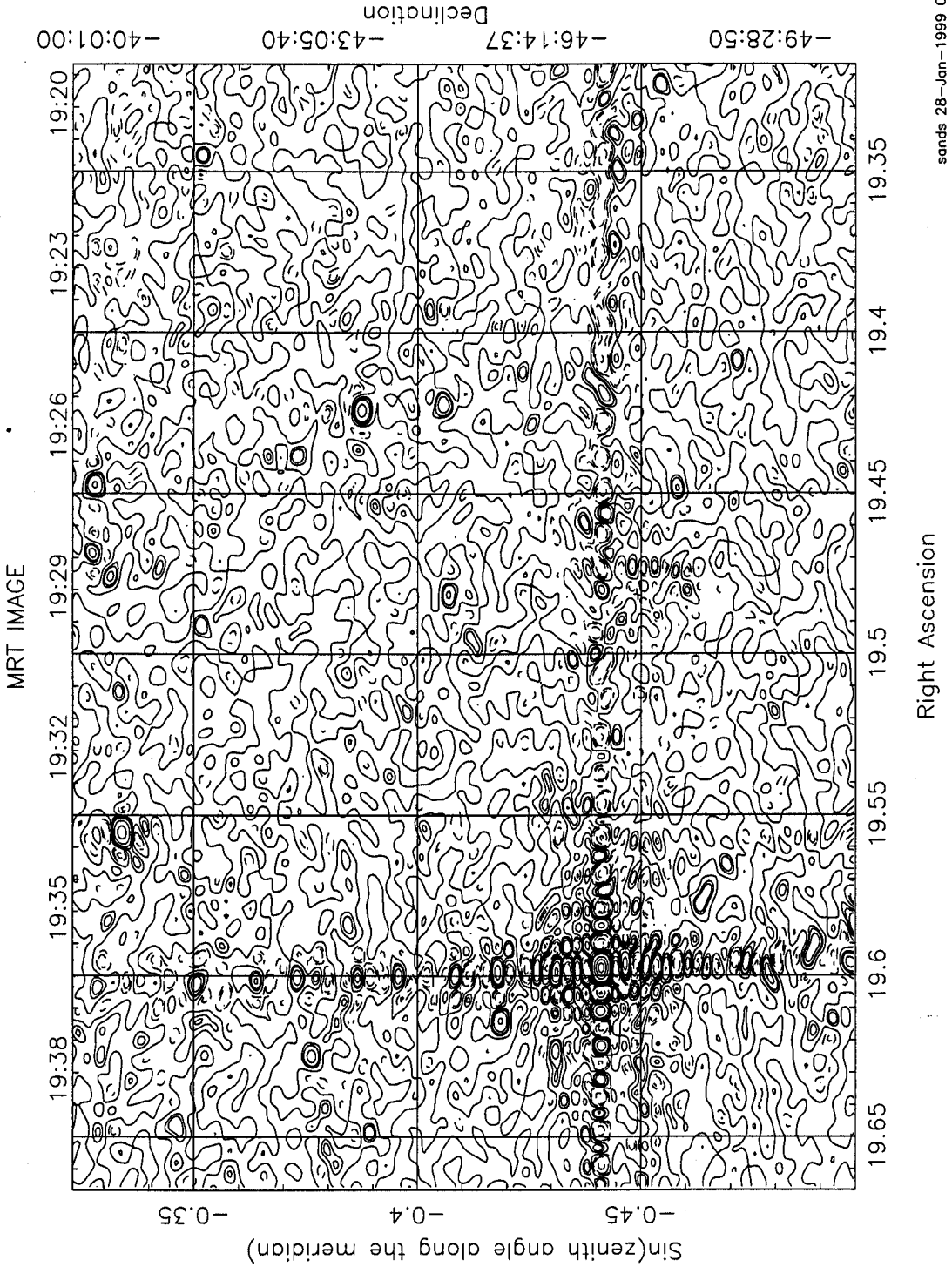
Figure 5.12: Map of the right ascension range (J2000) 19h19m to 19h40m and declination range (J2000) −50° to −39°.
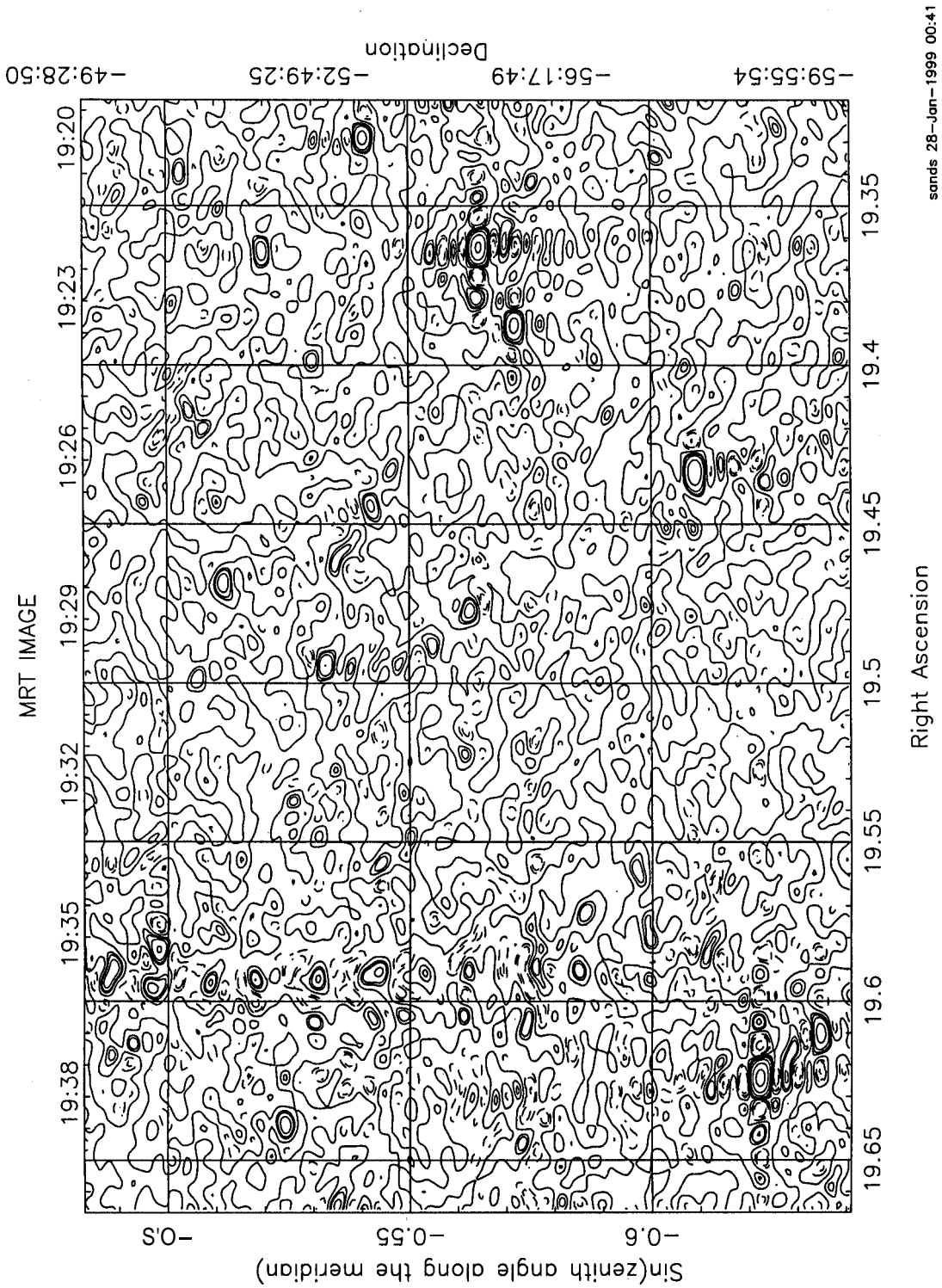
Figure 5.13: Map of the right ascension range (52000) **19h19m** to **19h40m** and declination range (52000) −60° to −49°.
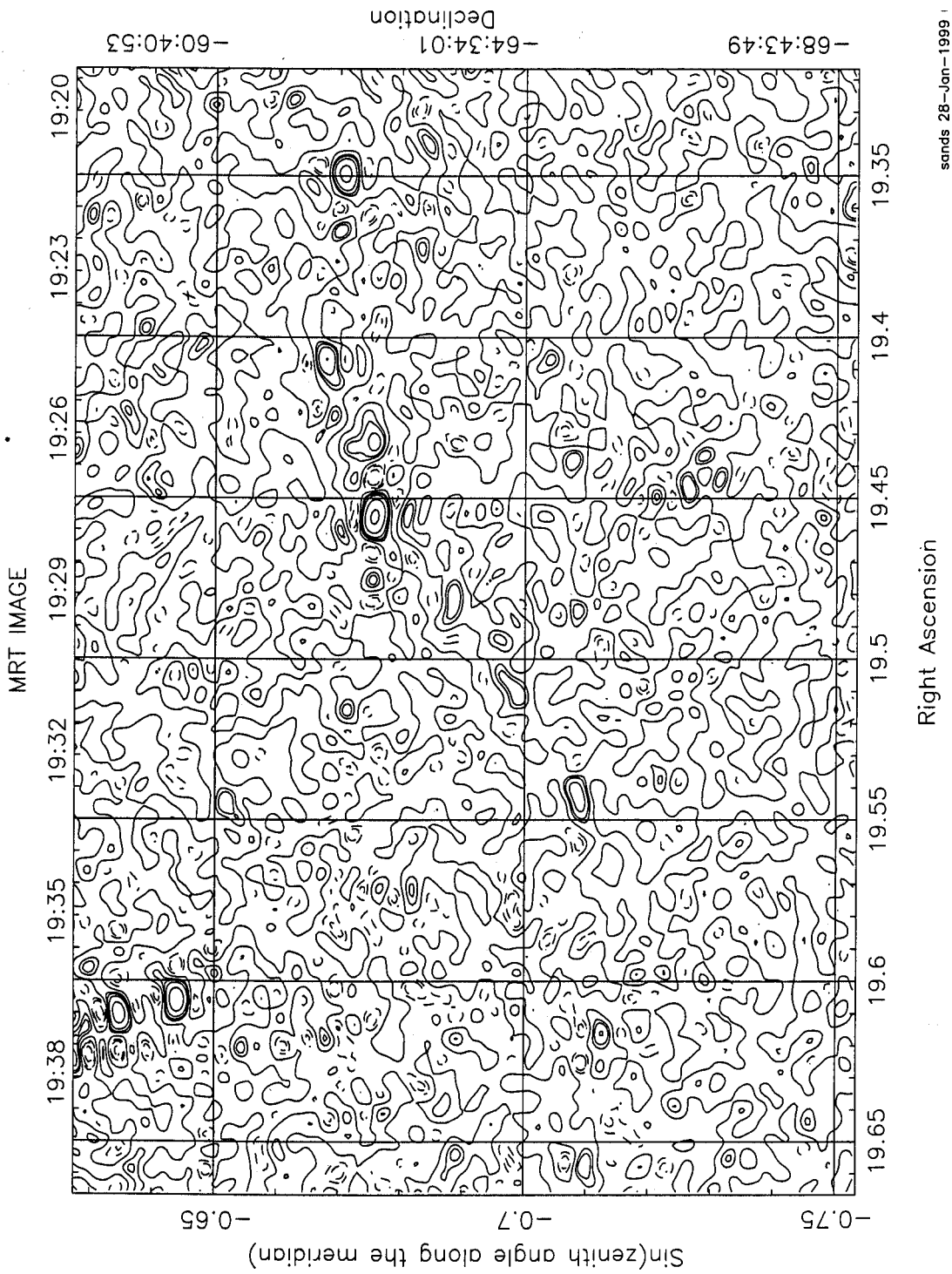
Figure 5.14: Map of the right ascension range (J2000) 19h19m to 19h40m and declination range (J2000) −70° to −59°.

Chapter 5: Images and their analysis
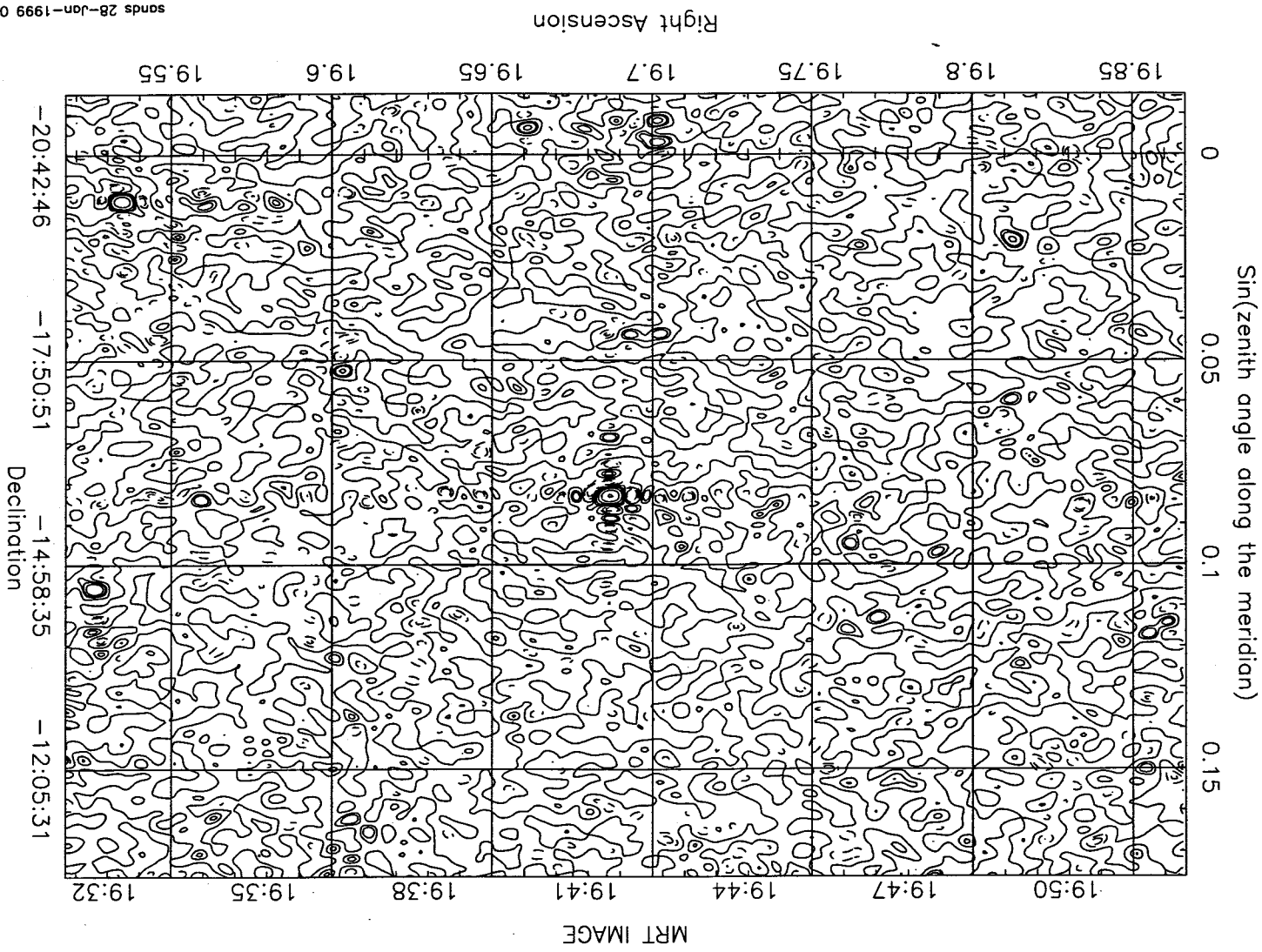
Figure 5.15: Map of the right ascension range (J2000) 19h31m to 19h52m and declination range (J2000) −21° to −10°.
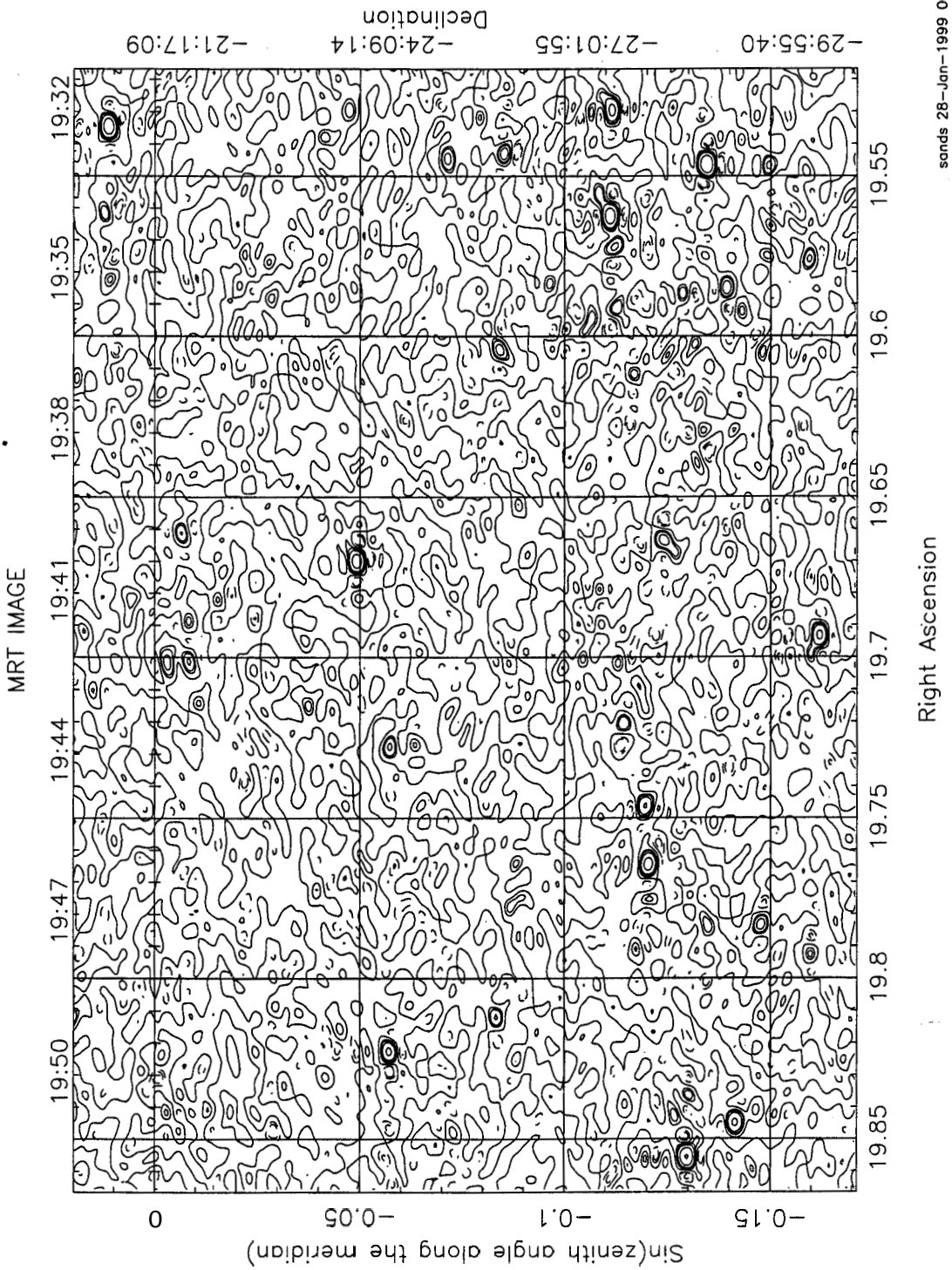
Figure 5.16: Map of the right ascension range (J2000) 19h31m to 19h52m and declination range (J2000) −30° to −19°.
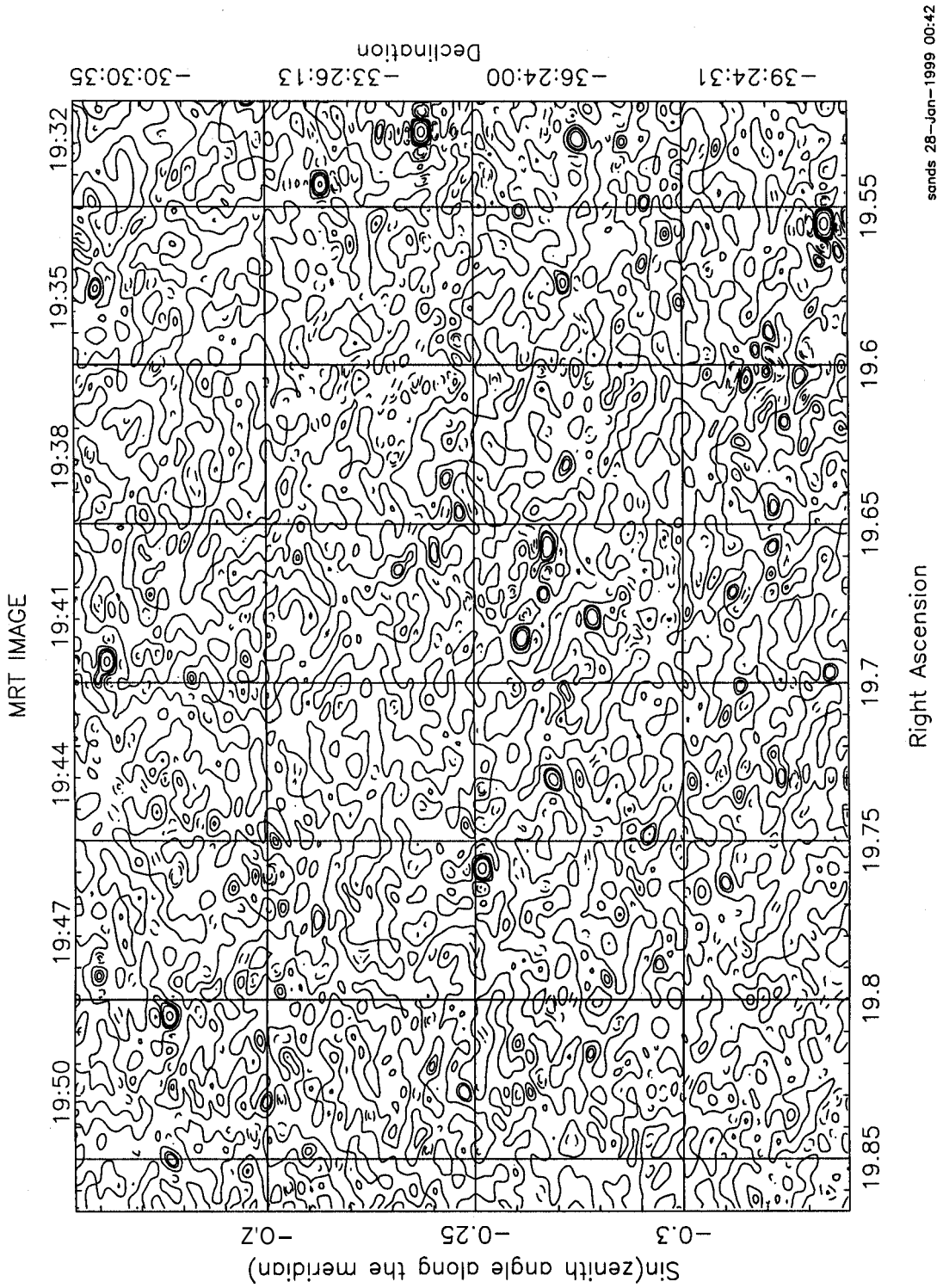
Figure 5.17: Map of the right ascension range (52000) 19h31m to 19h52m and declination range (52000) −40° to −29°.
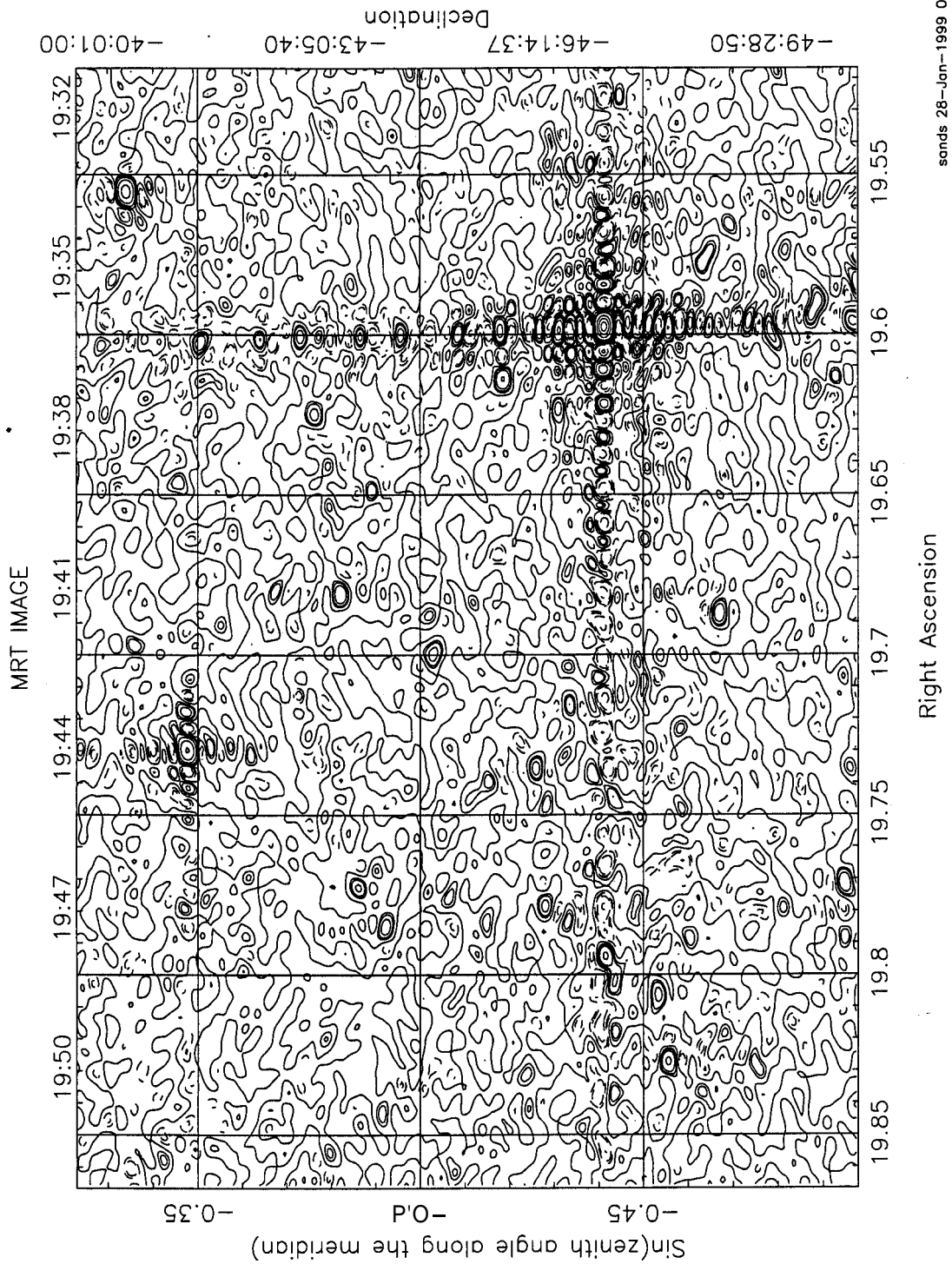
Figure 5.18: Map of the right ascension range (52000) 19h31m to 19h52m and declination range (52000) −50° to −39°.
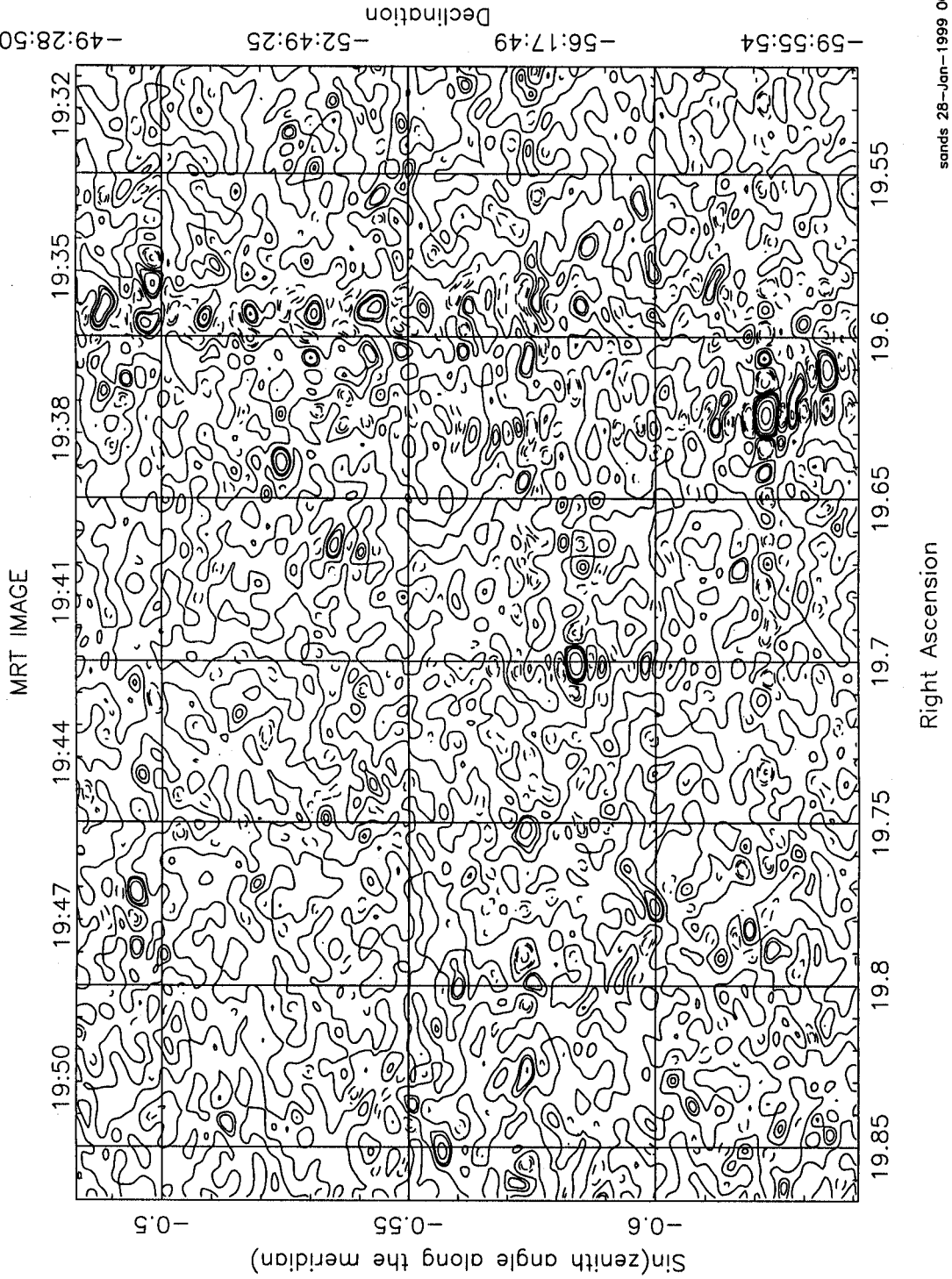
Figure 5.19: Map of the right ascension range (52000) **19h31m** to **19h52m** and declination range (52000) −60° to −49°.
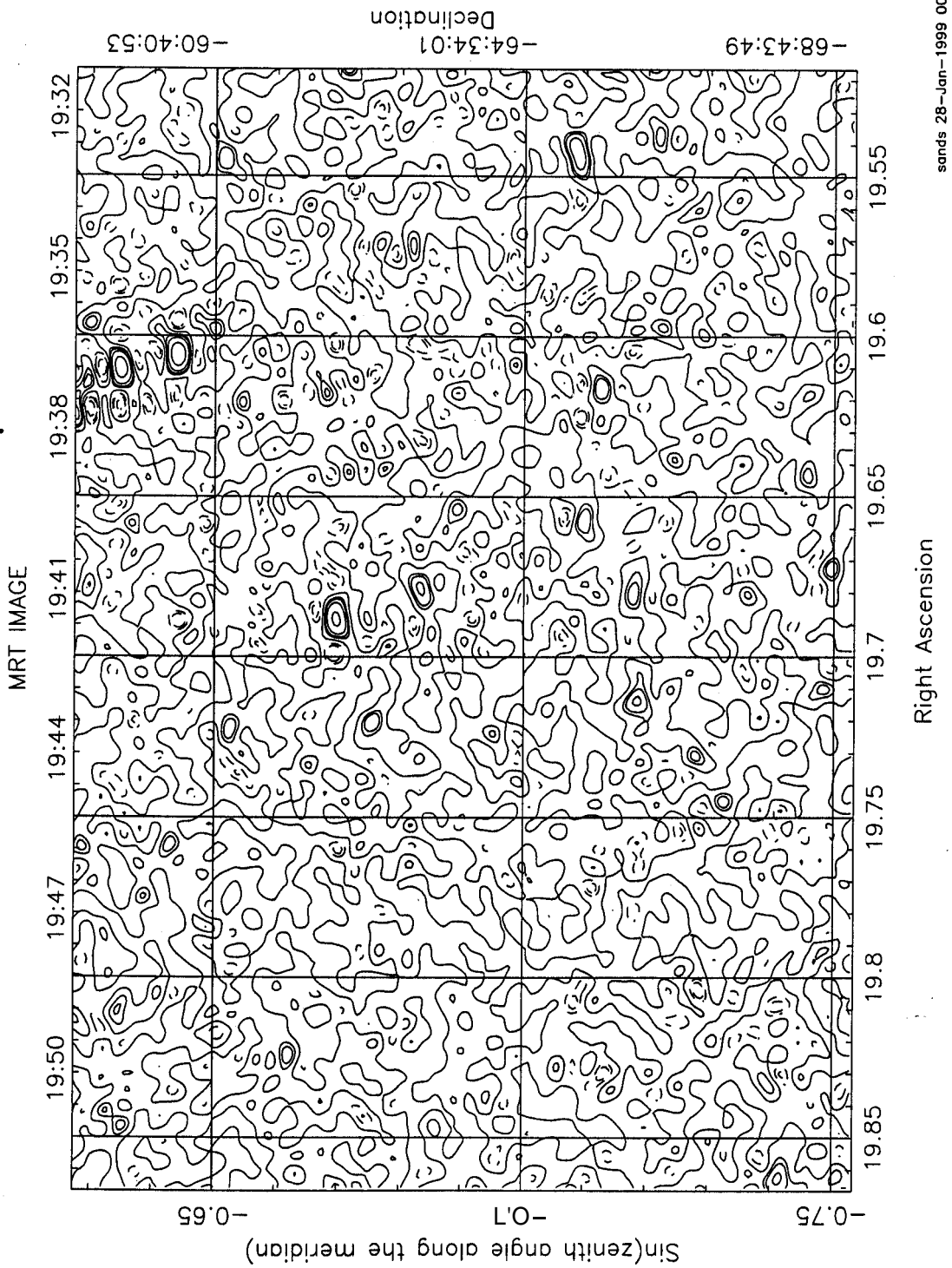
Figure 5.20: Map of the right ascension range (J2000) 19h31m to 19h52m and declination range (J2000) −70° to −59°.

In the second stage, the ratios of the MRT flux densities estimated from the images to that calculated from the Culgoora source list of 171 point sources common to the MRT and Culgoora source lists were found. Similarly the ratios of flux densities of 359 sources common to the MRT and the MRC were also found. For calculating the expected flux densities at 151.5 MHz from the Culgoora catalog and the MRC, a spectral index of 0.7 was assumed for all the sources used on the basis that most point sources are of extra galactic origin. The ratios of the flux densities as a function of declination were plotted. Since the flux densities are not corrected for the primary beam, this ratio follows the primary beam. To get the primary beam a cubic curve was fitted to this ratio. The fitted curve peaked at the declination of $-40°$ with an amplitude of 0.93. Therefore the flux densities had to be rescaled. The flux density of MRC 1932-464 was corrected to 87 Jy [18]. This is closer to the new estimate of 91 Jy at 160 MHz published by Slee in the corrected Culgoora catalog [41].

5.2.3   The images

Images from 19h02m to 19h57m in RA (J2000) are presented. The declination (J2000) coverage is from $-70°$ to $-10°$. The full declination image is a mosaic of parts of the four images made by combining data of different zones from different blocks. These parts are so chosen that the average decorrelation at any declination is less than 5%. The four images are labeled as L1, L2, L3 and L4 (Section 4.4). The different combinations of zones from different blocks used in each of these images are given in Table 4.3. The expected decorrelation in these four images is shown in Figure 4.34.

The full image has been split into 18 sub-images for display, each spanning 21 minutes in RA and 11 degrees in declination (Figure 5.3 to Figure 5.20)

	RA J2000	Dec J2000	Image used
Figure 5.3	19 02 00 19 23 00	−21° − 10°	L1
Figure 5.4	19 02 00 19 23 00	−30° − 19°	L2
Figure 5.5	19 02 00 19 23 00	−40° − 29°	L2
Figure 5.6	19 02 00 19 23 00	−50° − 39°	L3
Figure 5.7	19 02 00 19 23 00	−60° − 49°	L3
Figure 5.8	19 02 00 19 23 00	−70° − 59°	L4
Figure 5.9	19 19 00 19 40 00	−21° − 10°	L1
Figure 5.10	19 19 00 19 40 00	−30° − 19°	L2
Figure 5.11	19 19 00 19 40 00	−40° − 29°	L2
Figure 5.12	19 19 00 19 40 00	−50° − 39°	L3
Figure 5.13	19 19 00 19 40 00	−60° − 49°	L3
Figure 5.14	19 19 00 19 40 00	−70° − 59°	L4
Figure 5.15	19 31 00 19 52 00	−21° − 10°	L1
Figure 5.16	19 31 00 19 52 00	−30° − 19°	L2
Figure 5.17	19 31 00 19 52 00	−40° − 29°	L2
Figure 5.18	19 31 00 19 52 00	−50° − 39°	L3
Figure 5.19	19 31 00 19 52 00	−60° − 49°	L3
Figure 5.20	19 31 00 19 52 00	−70° − 59°	L4

Table 5.1: The full image has been split into 18 sub-images for display, each spanning 21 minutes in RA and 11 degrees in declination. The RA and declination coverage of the sub-images are summarized in this table

. The RA and declination coverage of the sub-images are summarized in Table 5.1. To avoid discontinuities each sub-image has overlapping boundaries with its adjacent ones. Figure 5.21 shows the expected decorrelation as a function of declination. Note that the overlapping boundaries do not always have identical decorrelations. Since these are dirty images, the corrections for the primary beam and for decorrelation have not been applied on the images displayed.The parameters of the images presented here are summarized in Table 5.2.
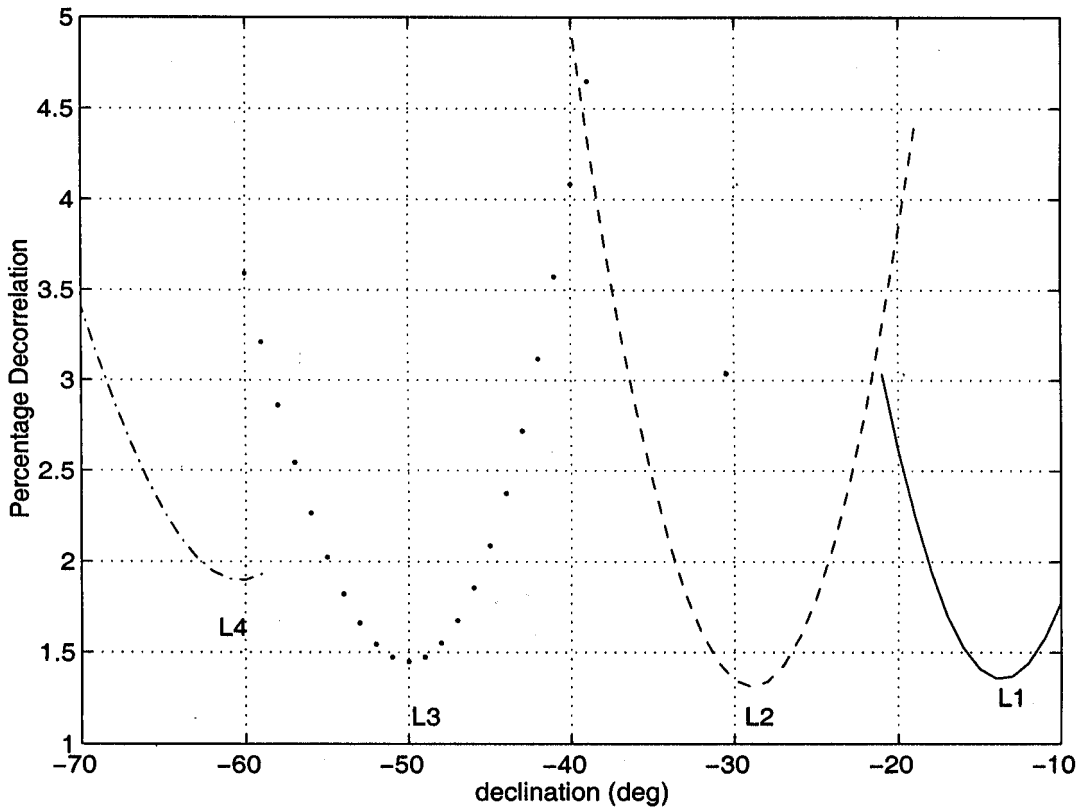
Figure 5.21: The expected decorrelation at different declinations.

About 600 interference points were detected in the RA range 19h02m to 19h52m. These points were given zero weighting while box-car averaging images of different days. There is practically no interference seen in the images presented here.

Observing frequency	151.5 MHz
Minimum and maximum baselines	2m, 441m
No of visibilities used per second	32 x 440 = 14080
Right ascension span	19h02m to 19h52m
Declination coverage	$-70°$ to $-10°$
Synthesized beam-width	4' x $9'.2 \sec(\delta + 20°.14)$
Point source sensitivity	550 mJy (1σ)

Table 5.2: Parameters of the images given in this thesis.

The strongest source in the images shown is our calibrator source MRC 1932-464 with a flux density of 87 Jy/beam at 151.5 MHz. The sidelobes of this source are seen all the way from 19h02m to 19h52m in RA and $-70°$ to $-10°$ in declination. The sidelobes in declination are seen to be curved, i.e., sidelobes at different declinations appear at the different right ascensions rather than at a single RA. This is due to the MRT array not being coplanar.

The images are presented in J2000 coordinates. The contour levels are $-1.2, -2.0, -4.0, -6.0, -8.0, -1.5, -2.0, -1.2, -0.8, +0.8, +1.2, +2.0, +4.0, +8.0, +15, +20, +40, +60, +80, +100$ Jy/beam.

5.3   Preliminary Analysis

5.3.1   Noise in the images

We estimated the noise in the images made with 4 seconds of integration. To estimate the noise in these images, we selected regions which appeared to be devoid of sources. The RMS measured in several such regions were then averaged to get an estimate of the noise. This is about 550 mJy.

The expected noise, ΔS_{min}, is given by (Equation 2.8):

$$\Delta S_{min} = \sqrt{\left(\frac{\sqrt{2}\, 2k_B(\sqrt{T_{sys_{ew}}T_{sys_{ns}}})}{\eta_{eff}\sqrt{N_b}A_e\sqrt{\Delta\nu t}}\right)^2 + S^2_{conf}}$$

In the above equation, to calculate the system noise one needs to know the system temperature. An estimate of the system temperature at the RA imaged was obtained by convolving the 408 MHz image with the beams of the elements of the interferometer (east-west group and a north-south trolley) and using a temperature spectral index, α_T (T $\propto \nu^{-\alpha_T}$) of 2.7 for regions away from the galactic plane. The variation in system temperature with RA is shown in Figure 5.22. From this plot, at an RA of 19h, the brightness temperature of an east-west group is about 850 K and of a north-south trolley is about 800 K . Since the receiver temperature is about 400 K, the system temperature, $T_{sys} = \sqrt{T_{sys_{ew}}T_{sys_{ns}}}$ is about 1200 K. The confusion noise expected is ~35 mJy. Substituting these in the above equation[6] we get an RMS (1σ)of ~300 mJy. Since the images under consideration are not deconvolved there will be contributions from the sidelobes of various sources in the estimation of the RMS noise in the images. To estimate the contribution from the sidelobes of sources, we formed an image in the RA range 19h02m to 19h52m by convolving all sources listed in the MRC with the synthesized beam of the MRT. Sources in the RA range 18 hrs to 21 hrs and in the entire declination range of MRC ($-85° \leq \delta(1950) \leq -18.5°$, $|b| \geq 3°$) were used. We chose sources from a region much larger than the region of interest to minimize edge effects of convolution and to ensure inclusion of sidelobes of sources which are outside the region imaged. In this image, the contribution due to the sidelobes was found to be ~80 mJy/beam in a region away from most bright sources. Addition of this noise in quadrature to 300 mJy/beam gives 310 mJy/beam. This still does not explain the 550 mJy/beam noise measured in our image. To eliminate the possibility of noise in a small set of baselines dominating the

---

[6]$k_B = 1.3805 \times 10^{-23}$, $\eta_{eff} = 0.81$, $N_b = 32 \times 440 = 14080$, $A_e = 2\sqrt{A_{ns}A_{ew}} = 2\sqrt{16 \times 128} = 90.5\ m^2$, $\Delta\nu$=1 MHz, t=4 seconds.

measured noise in the images, the noise was also estimated in the images made using data of each block. Table 5.3 gives the noise measurement in the images in each block along with the theoretically expected values. We see that the noise in the images of each block is about the same $(1.5\pm0.2$ Jy). The noise is much higher than the theoretically expected receiver noise. We initially assumed that the remaining component was due to confusion noise. However, by adding different images we find that the,noise in them behaves like thermal noise, i.e., goes down by $\sqrt{N}$ on averaging N images. The other thing we need to consider in calculating the noise is the contribution from the undetected interference in the images. It is not quite straightforward to estimate the contribution of this factor to the total noise. However, assuming that there is undetected interference at each sidereal second in the data of only one of the days used to make the images, the ratio of undetected interference to noise in the images made with N days of data is $\approx 2.83\sqrt{\frac{T_{integ}}{N}}$ (Section 4.1). For 30 days of data that we have used in this image, with an integration time of 4 seconds, this ratio is about one. Therefore the total noise in the image due to contributions from receiver noise, sidelobes of sources, undetected interference and confusion would be $\sqrt{300^2 + 80^2 + 300^2} \approx 450$ mJy. This leaves out about 20% of the noise to unaccounted.

Block	Measured RMS noise	Expected receiver noise	Confusion noise
block1 (6 m - 94 m)	1.5 Jy	0.6 Jy	?
block2 (2 m - 5 m, 95 m - 171 m)	1.4 Jy	0.6 Jy	?
block3 (172 m - 261 m)	1.6 Jy	0.6 Jy	?
block4 (262 m - 351 m)	1.7 Jy	0.6 Jy	?
block5 (352 m - 441 m)	1.5 Jy	0.6 Jy	?

Table 5.3: Noise measured on images at different stages.
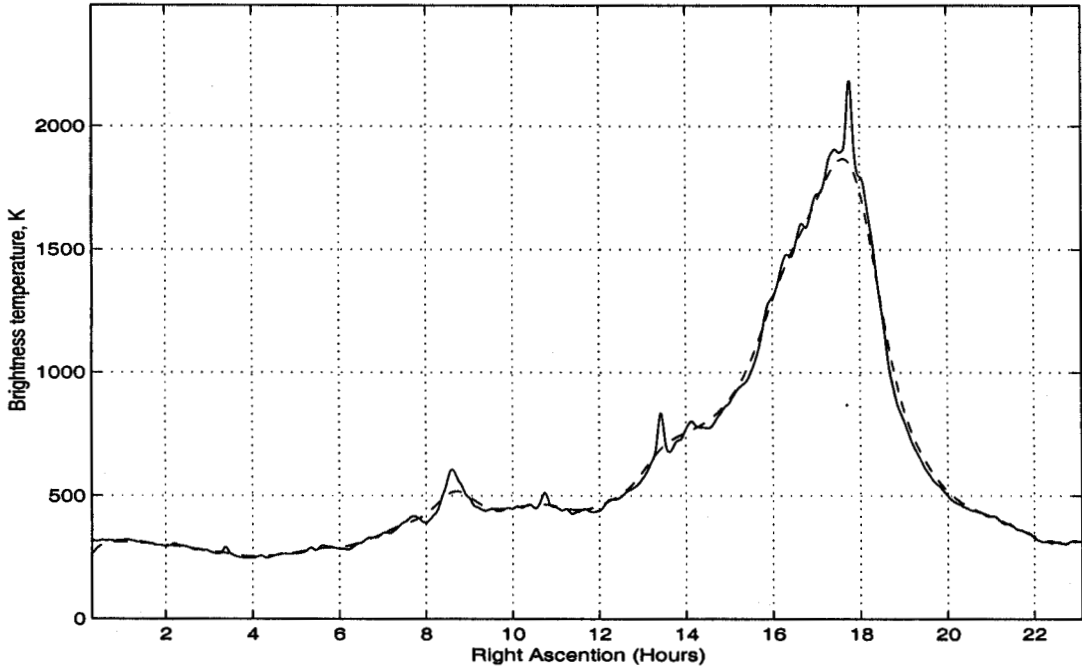
Figure 5.22: Estimate of the variation of the system temperature with RA obtained by convolving the 408 MHz image with the beams of an east-west group (solid line) and a north-south trolley (dashed line). A temperature spectral index of 2.7 is used.

5.3.2   Estimation of positions and flux densities of sources

Our aim was to estimate the 151.5 MHz flux densities and the positions of the sources given in the MRC. There are 54 sources in the MRC in the RA range 19h02m to 19h52m which are expected[7] to have a flux density $S_{150} \geq$ 3 Jy/beam (5σ) in the MRT field of view. Out of these we have been able to detect 53 sources. These are listed in Table 5.4 and Table 5.5. MRC 1934-63 was not detected in our image. We discuss more about this undetected source later in this section. The source position and its strength was obtained by doing a least square fit of the expected beam around the position given in the MRC.

Positional discrepancies with respect to the MRC source positions are ob-

---
[7]Assuming a spectral index of 0.7.

Source Number	Right ascension (J2000)	Declination (J2000)	Flux density S_{150}, Jy	MRC identification
1.	19h02m39	-27d05m53	9	MRC 1859-271
2.	19h02m49	-23d29m51	22	MRC 1859-235
3.	19h07m48	-53d08m04	5	MRC 1903-532
4.	19h11m40	-17d12m08	4 ·	MRC 1908-172
5.	19h14m19	-55d05m59	7	MRC 1910-551
6.	19h14m44	-55d59m14	4	MRC 1910-560
7.	19h14m28	-29d28m19	6	MRC 1911-295
8.	19h15m47	-26d53m03	17	MRC 1912-269
9.	19h17m39	-45d30m29	8	MRC 1914-455
10.	19h17m54	-12d04m37	7	MRC 1915-121
11.	19h19m28	-29d58m05	10	MRC 1916-300
12.	19h21m52	-54d31m51	18	MRC 1917-546
13.	19h21m55	-35d26m46	8	MRC 1918-355
14.	19h24m11	-15d48m58	4	MRC 1921-159
15.	19h24m51	-29d14m29	5	MRC 1921-293
16.	19h26m06	-57d39m47	8	MRC 1921-577
17.	19h25m30	-42d57m38	5	MRC 1921-430
18.	19h27m27	-62d39m30	12	MRC 1922-627
19.	19h25m58	-18d36m46	7	MRC 1923-187
20.	19h26m28	-32d42m41	10	MRC 1923-328
21.	19h26m55	-39d17m43	5	MRC 1923-393
22.	19h27m24	-22d58m49	5	MRC 1924-230
23.	19h27m38	-28d10m44	6	MRC 1924-282
· 24.	19h28m19	-29d31m48	8	MRC 1925-296
25.	19h29m08	-37d32m52	6	MRC 1925-376
26.	19h29m22	-36d13m44	3	MRC 1926-363

Table 5.4: List of sources in the RA range 19h02m to 19h30m with their position, flux density and MRC source identification

Source Number	Right ascension (52000)	Declination (52000)	Flux density S_{150}, Jy	MRC identification
27.	19h30m22	-35d50m46	5	MRC 1927-359
28.	19h30m01	-15d09m13	11	MRC 1927-152
29.	19h31m38	-33d54m36	10	MRC 1928-340
30.	19h31m48	-36d07m00	3	MRC 1928-362
31.	19h31m35	-14d06m00	7	MRC 1928-142
32.	19h32m07	-19d31m49	10	MRC 1929-196
33.	19h32m38	-32d29m44	4	MRC 1929-326
34.	19h32m50	-27d54m04	8	MRC 1929-280
35.	19h33m23	-39d40m20	10	MRC 1929-397
36.	19h33m48	-26d33m30	7	MRC 1930-266
37.	19h36m25	-60d14m00	8	MRC 1932-603
38.	19h35m57	-46d20m43	87	MRC 1932-464
39.	19h36m42	-59d33m18	7	MRC 1932-596
40.	19h37m32	-58d38m25	23	MRC 1933-587
41.	19h36m58	-44d54m28	4	MRC 1933-450
42.	19h41m21	-62d11m25	6 ·	MRC 1936-623
43.	19h40m13	-22d59m45	8	MRC 1937-231
44.	19h41m16	-47d59m54	3	MRC 1937-481
45.	19h42m06	-55d53m30	8	MRC 1938-560
46.	19h41m15	-15d24m31	26	MRC 1938-155
47.	19h43m52	-40d30m10	15	MRC 1940-406
48.	19h44m50	-27d02m53	5	MRC 1941-271
49.	19h45m35	-34d45m00	5	MRC 1942-348
50.	19h45m54	-27d06m28	6	MRC 1942-272
51.	19h48m22	-30d20m15	4	MRC 1945-304
52.	19h49m24	-23d27m09	6	MRC 1946-235
53.	19h51m23	-27d37m20	9	MRC 1948-277

Table 5.5: List of sources in the RA range 19h30m to 19h52m with their position, flux density and MRC source identification.

tained from the least square fit. The discrepancies in RA and declination plotted against the strength of the source are shown in Figure 5.23 and Figure 5.24 respectively. Since the declination beam gets broader at larger zenith angles along the meridian, the discrepancy in declination are given as equivalent discrepancy at the zenith. The histograms of the positional discrepancies with RA and declination are shown in Figure 5.25 and Figure 5.26 respectively. The positional discrepancy in declination is within 2 arcmin. The positional discrepancy in RA is within 0.8 arcmin. We find no systematic discrepancy in position either with declination or with right ascension.

We also carried out positional analysis on artificial point sources of various strengths which were added to the images at different places. The positional errors in these detection were within 1.5 arcmin in declination and 0.7 arcmin in RA. The position and strength of the sources used for this simulation were derived from the MRC source list in the right ascension range 18 hrs to 19 hrs.

Figure 5.23: Plot showing discrepancy in RA with source strength.
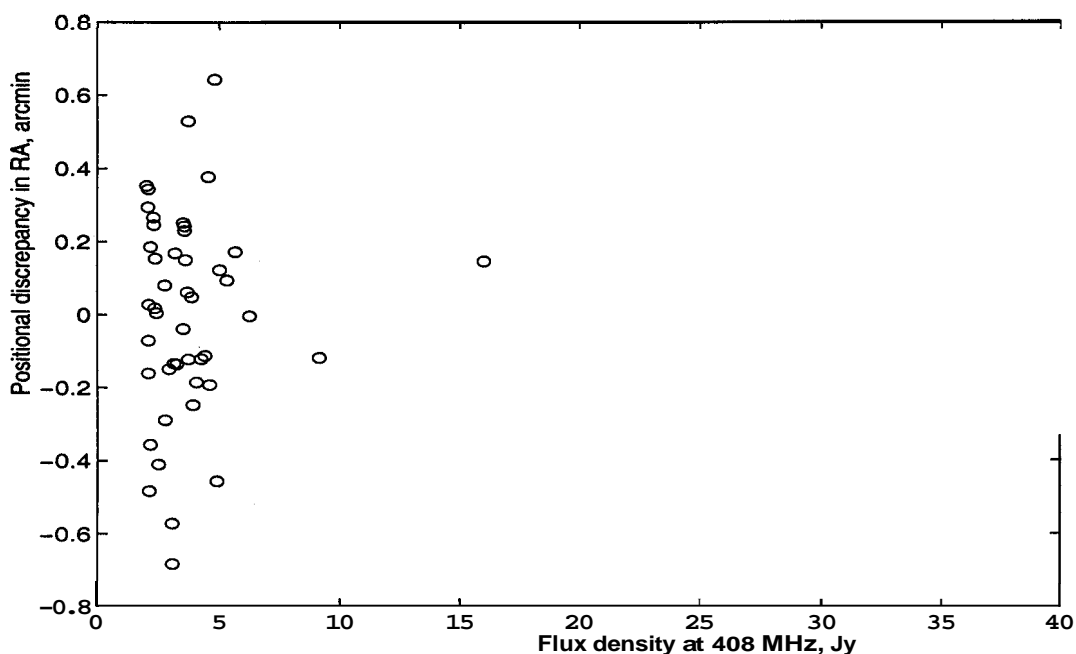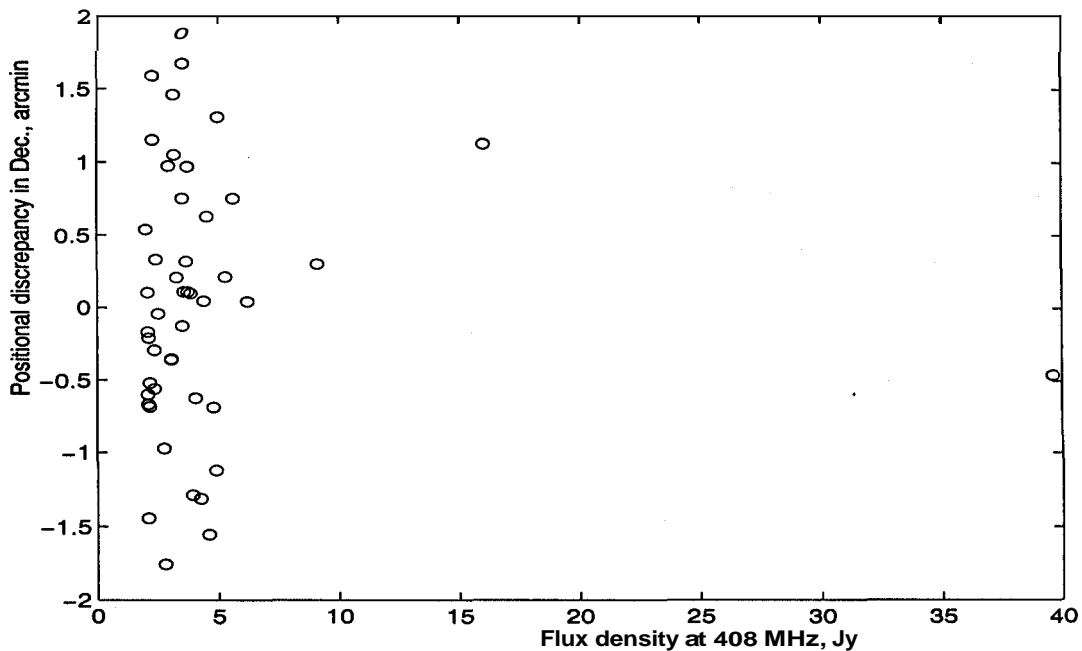
Figure 5.24: Plot showing discrepancy in declination with source strength.

The flux densities of the sources, with corrections for the primary beam, are given in Table 5.4 and Table 5.5. From the ratio of the measured flux density to the expected flux density we get an estimate of the primary beam. The deviation of this estimated primary beam from the theoretical primary beam is always less than 10% in the declination range of interest. Figure 5.27 shows the ratio of measured flux density to the expected flux density with declination. The solid line in this figure shows the theoretical primary beam and the broken line shows the best-fit. Figure 5.28 shows the spectral index of the sources detected. The spectral index are derived from the flux density measurements at 151.5 MHz in our image and the flux densities at 408 MHz given in the MRC. Apart from two sources which seem to have a very flat spectrum, the spectral index are in the range ~ 0.4 to ~ 1.4. The sources with flat spectrum in this frequency range are MRC 1908-172 and MRC 1921-293[8].

[8]From [44]: "MRC1921-293 is one of the strongest sources in the sky at millimeter wave-
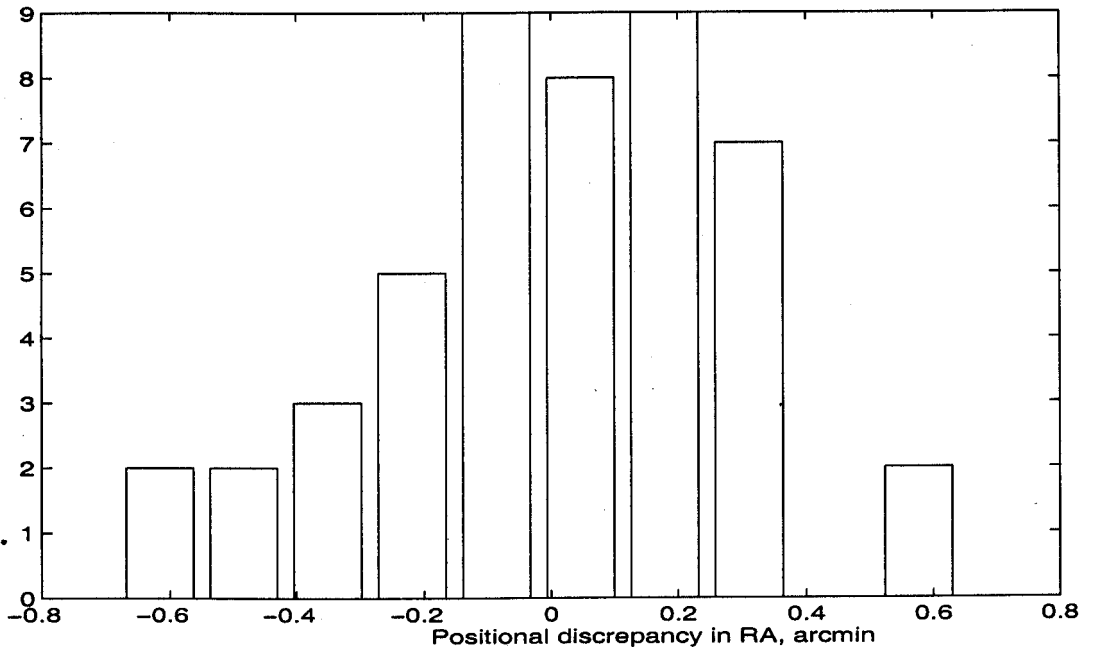
Figure 5.25: Histogram of discrepancy in RA.

From the flux density measurements in each of the four images L1, L2, L3 and L4 we estimate the bandwidth decorrelation in these images. Figure 5.29 shows the decorrelations estimated in the images from the measurements along with the expected decorrelation curves.

As mentioned earlier in this section, MRC 1934-63 is the only source not detected out of the list of 55 expected sources. It has a flux density of 6.2 Jy at 408 MHz. We did not detect this source in the image made with 4 seconds of integration. The expected flux density of this source at 151.5 MHz using a

lengths and has an unusually flat spectrum between 1 mm and 1 m. At shorter wavelengths, the spectrum steepens and continues with a spectral index a 1 out to at least ultraviolet wavelengths (Shen et al. 1998a). The secondary feature is unusually diffuse. VLBA observations made at 7 mm in 1994 and in 1996 (Shen, Moran and Kellermann 1998b) show that the jet curves sharply and is elongated along a position angle near $-23°$ out to a distance of about 1 mas (**4** pc), where there is an extension in the 7 mm image toward the diffuse jet that we see at 2 cm located about 6 mas away. Observations at 6 cm made in 1996 are consistent with the 7 mm and 2 cm observations, but 6 cm observations made in 1992 by Shen et al. (1998a) show a secondary feature that lies to the northwest rather than the northeast of the core. Curiously, there is no reported gamma-ray emission from this, one of the brightest known blazars (Mattox et al. 1997)."
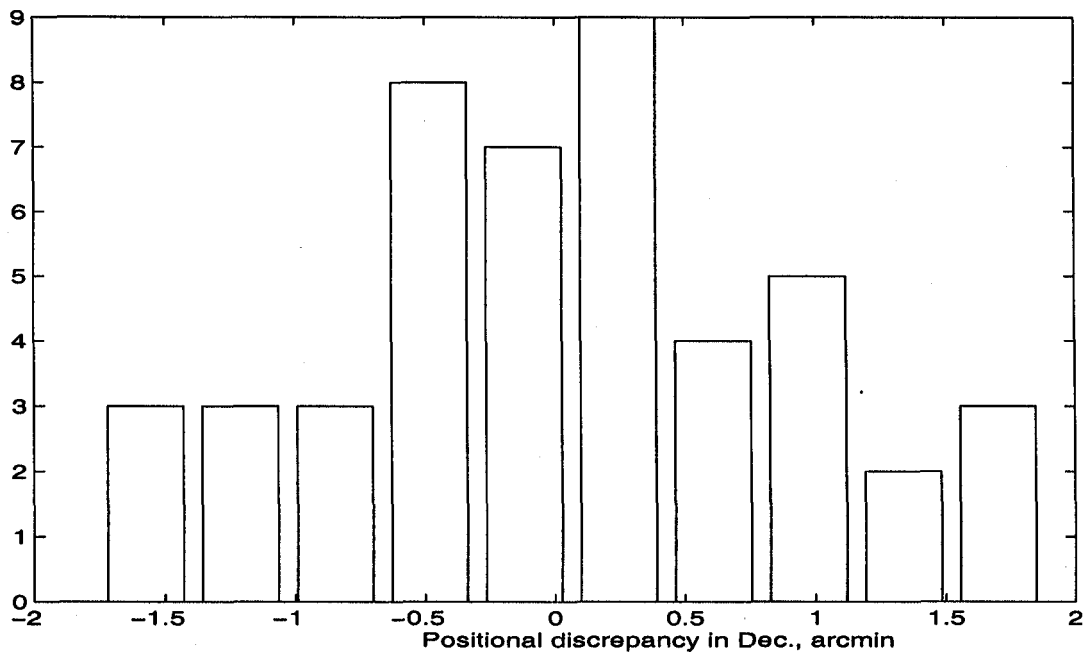
Figure 5.26: Histogram of discrepancy in declination.

spectral index of 0.7 would be 12.4 Jy. From the literature available we find that the spectrum of this source source has a turnover at around 1 GHz. It has flux densities of 13.65 Jy at 843 MHz (MOST), 16.4 Jy at 1400 MHz (NVSS), 11.1 Jy at 2700 MHz (Parkes) and 5.9 Jy at 5000 MHz (PMN). The flux densities at different frequencies for this source are shown in a log-log plot in Figure 5.30. From this plot we get the spectral index close to 0.8 for frequencies beyond 1400 MHz and a spectral index close to -1.1 for frequencies between 408 MHz and 843 MHz. If we assume that the spectral index -1.1 for frequencies down to 151.5 MHz, the expected flux density at 151.5 MHz would be about 2 Jy. Since this source is at the half power point of the helix primary beam we would expect to see it as a 1 Jy source in our image. We have a probable detection at 2σ level (1 Jy) at this position. This detection needs to be confirmed.

It will be interesting to look for sources in our image which are not detected
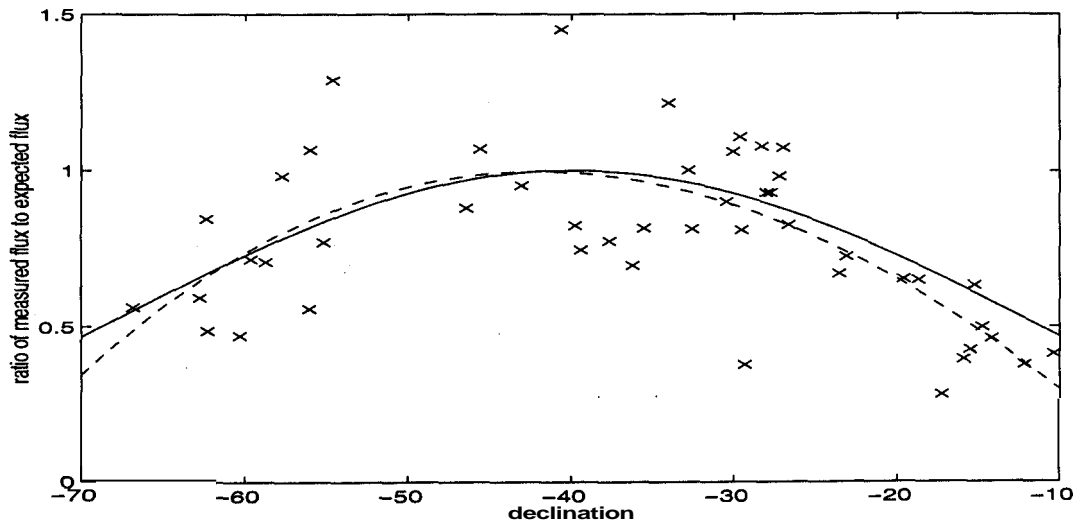
Figure 5.27: Plot showing ratio of measured flux density to the expected flux density. The solid line shows the theoretical primary beam and the dashed line shows the best-fit.

in the MRC. A cursory glance reveals there are many such sources. These were detected by displaying an image with only the point sources from the MRC convolved with the MRT beam and our image alternately on the screen (blink mode in AIPS). The additional sources were visually picked up. A further study of these sources is underway.
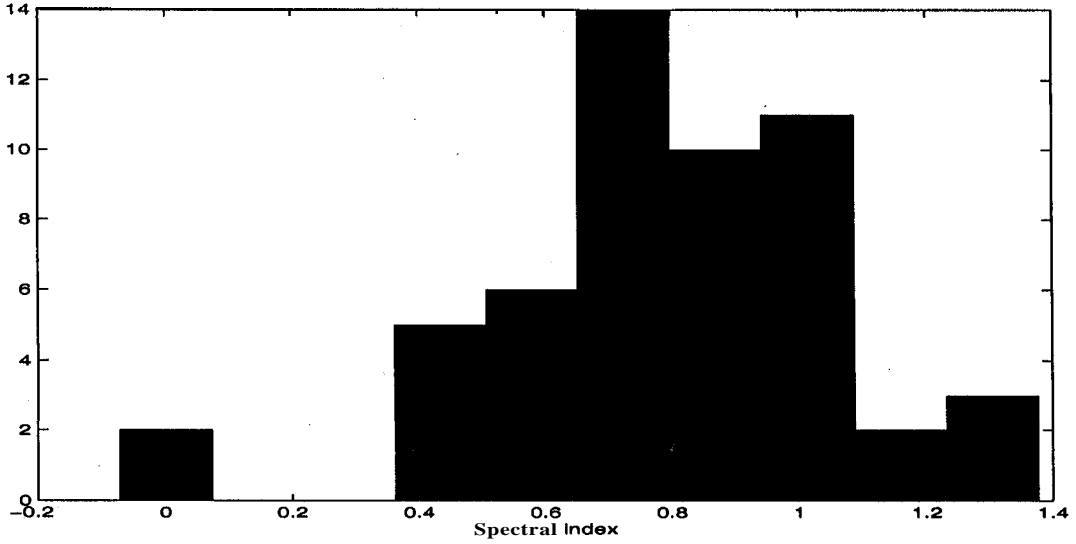
Figure 5.28: Histogram of spectral index of the sources detected for frequencies between 151.5 MHz and 408 MHz.
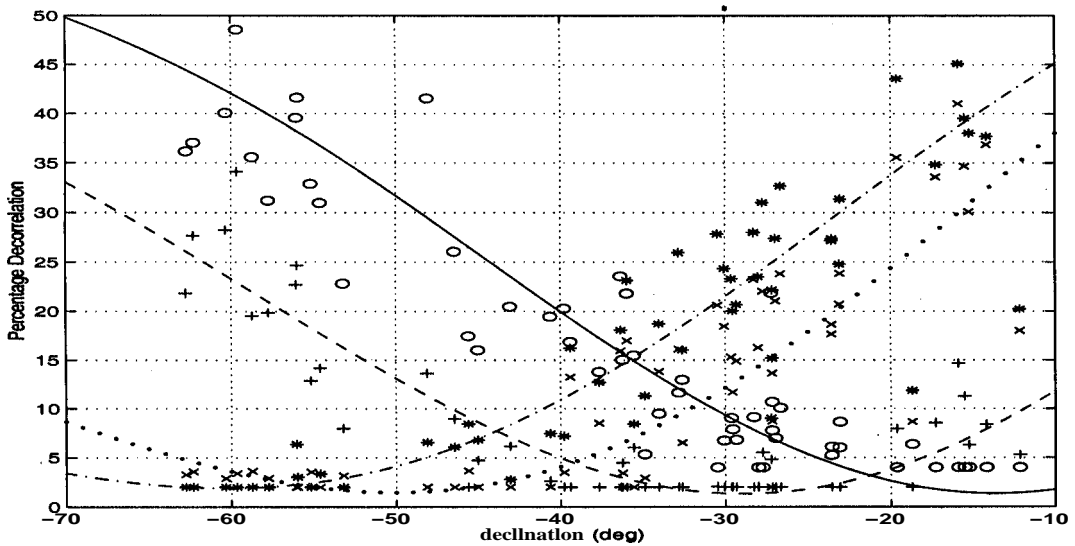
Figure 5.29: The decorrelation estimated from the measurements for the different images are plotted. The expected decorrelation curves are overlaid. o points and the solid line are for L1, **+** points and the dashed line are for L2, x and the dotted line are for L3, * and the dash-dot line are for L4.
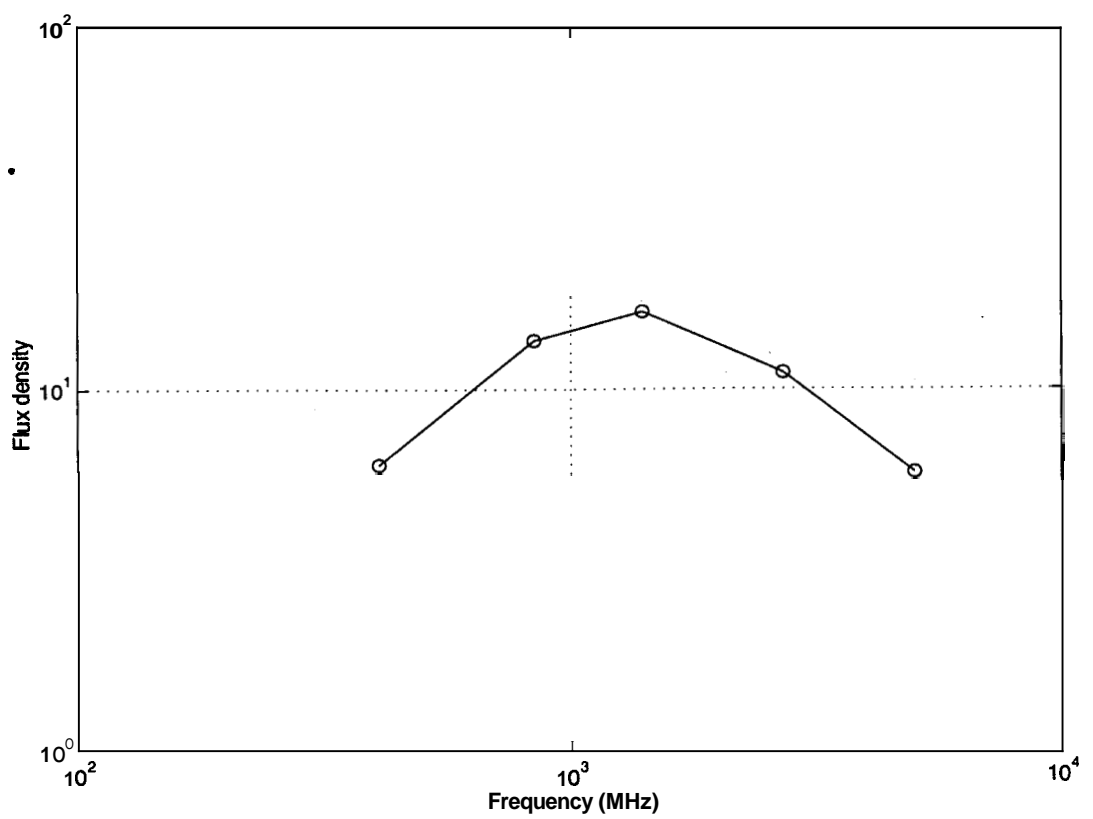
Figure **5.30:** Spectra of MRC **1934-63.**